Size-Dependent Optical Properties of Metallic Nanostructures

5

Lucía B. Scaffardi, Daniel C. Schinca, Marcelo Lester,
Fabián A. Videla, Jesica M. J. Santillán, and
Ricardo M. Abraham Ekeroth

Contents

1 Definition of the Topic

Metallic nanostructures are a key component of current and future nanotechnology devices since their individual properties convey the appropriate characteristics for applications in several fields of science and technology. At the nanoscale size,

L.B. Scaffardi (✉) • D.C. Schinca • F.A. Videla • J.M.J. Santillán
Centro de Investigaciones Ópticas (CIOp), CONICET La Plata-CIC, La Plata, Argentina

Departamento de Ciencias Básicas, Facultad de Ingeniería, Universidad Nacional de La Plata, La Plata, Argentina

M. Lester • R.M.A. Ekeroth
Grupo de Óptica de Sólidos-Elfo, Centro de Investigaciones en Física e Ingeniería del Centro de la Provincia de Buenos Aires – Instituto de Física Arroyo Seco, Facultad de Ciencias Exactas, Universidad Nacional del Centro de la Provincia de Buenos Aires, Buenos Aires, Argentina

Consejo Nacional de Investigaciones Científicas y Técnicas CONICET, Buenos Aires, Argentina

optical properties of metal structures depend not only on the type of material but also on the dimensions and geometry of the structure, suggesting the possibility of tuning optical resonances through appropriate engineering. In this chapter, we will describe methods for calculation of size-dependent optical properties of metal nanostructures and show the successful use of extinction spectroscopy technique to determine the size of nanoparticles (Np/Nps).

2   Overview

From a classical point of view, the optical properties of materials are condensed in the so-called constitutive parameters, namely, the electric permittivity and the magnetic permeability. Particularly, the dielectric function condenses the averaged response of the constitutive electrons of matter to an externally applied electric field. If this electric field varies in time, the dielectric function not only integrates the electron characteristics of the specific material but it will also depend on the frequency of the incoming field.

For metals at the nanoscale, the dielectric function behaves differently from its macroscopic (bulk) counterpart, since the electrons start to show confinement effects. This behavior includes an explicit dependence on particle size. In turn, the optical absorption, scattering, and extinction cross sections are functions of the metal dielectric function, thus translating the size dependence to the optical properties of the metallic nanostructure.

In this chapter, we overview the contribution of free and bound electrons to the metal dielectric function and apply different theoretical approaches to the calculation of optical extinction spectra of nanowires, nanotubes, and bare and core-shell nanoparticles. We then apply these results to fit experimental extinction spectra and determine the size of nanostructures which compare very well with high-resolution TEM.

3   Introduction

The developments in the nanotechnology area have been undoubtedly one of the greatest achievements of science in the late twentieth century. The particular interest in understanding the physical and chemical phenomena associated with nanoscale systems (clusters of several tends of atoms up to systems with characteristic distances of small fractions of a micron) is mainly due to its high technological potential. Nanotechnology has found wide applications in broad interdisciplinary science fields. We found significant developments in the biomedicine area, lasers, communications, and medical physics, to name a few.

This increasing trend toward nanoscience and nanotechnology makes it inevitable to study the optical properties and electromagnetic response (near and far field, resonances) on the nanometer scale. In particular, over the last two decades, the interest in metallic clusters, metallic nanoparticles (core-shell systems, nanowires), and systems with nanometric details has grown significantly ([1–15], and therein).

The term "nanoparticle" includes from small clusters, size range around 1 nm (tens of atoms), up to particles consisting of hundreds of thousands of atoms (or even greater) and having a diameter in the range of tens to hundreds of nanometers. In the literature, this kind of material has long been known as colloids, generally applied to suspensions of metal particles in an aqueous medium. In fact, colloidal gold has been used as a coloring pigment dating back to the Middle Ages [7].

The excitation at optical frequencies of "eigenmodes" (surface plasmon resonances in metallic nanoparticles, whispering gallery modes in the dielectric spheres, and other resonant phenomena) is probably one of the most spectacular electromagnetic effects in nanosystems. In particular, plasmon resonances lead to extremely strong fields in the vicinity of a nanoparticle. Such fields play, for example, a key role in surface-enhanced Raman scattering, wherein the Raman signal of a molecule deposited on the nanoparticle is enhanced by several orders of magnitude [16]. This enhancement can be large enough that the Raman spectrum of a single molecule can be detected [17, 18].

The large extinction cross section associated with plasmon resonances also produces a strong signal in the far field. This observation is the key to detect and investigate optical properties of nanoscopic particles. Plasmon resonance occurs for specific wavelengths and gives the particles ensemble its color. These resonance frequencies are sensitive not only to particle size but also its shape. The properties of the metal particles were used during the Middle Ages for the design of colored glass. This was mostly an empirical art, close to alchemy, where the relation between the metallic particle shape and its color (its spectrum of plasmon resonances as it is called today) was only known by the master glass-makers. In the nineteenth century, Faraday noted that there must be a relationship between the ruby red color of a colloidal gold suspension and the presence of aggregates of metal atoms, although he had no means of analyzing the size of these metallic nanoparticles by modern analytical techniques such as transmission electron microscopy (TEM).

The theoretical investigation of this problem remained however extremely limited. The exact treatment of the problem of scattering of electromagnetic waves by particles is limited only to a few very simple geometries such as spheres or ellipsoids in 3D, or a nanowire with a cylindrical or elliptical section in 2D [19–24]. In general, for simple situations, it can be solved using Mie theory or related semi-analytical techniques. Recently, through discrete dipole approximation or finite element approaches, it is possible to calculate the electromagnetic interaction between particles of different shapes and sizes. However, these calculations become very difficult when the particle size is smaller than 20 nm, extremely rapid variations of the field occur on very short distances. Using these techniques to study the resonance spectra of silver nanowires with a non-regular cross section, it was shown that nanowires had a complex spectrum, with many different resonances [25]. In particular, triangular wires seem to produce the most complex spectrum, as it was demonstrated in [26, 27], where nanowires with different convex polygonal sections were systematically investigated.

An interesting question that arises when studying the interaction of electromagnetic waves with nanoscale systems is about the validity of Maxwell's equations for these scales. The constitutive parameters characterize completely the system, but they are calculated for "macroscopic bodies." They represent an averaging of quantum phenomena that occur during the interaction over a large number of atoms to achieve an adequate bulk representation.

In general, for metals with characteristic dimensions on the order of the wavelength or larger, the bulk atoms contribute mainly to the dielectric function. For example, for systems with few cubic millimeters, the relationship between surface atoms and bulk atoms is less than 10^{-3}. When the volume is a few tens of nanometers, the relationship is about 0.1. However, for systems with few nanometers of characteristic dimensions, all atoms can be considered like surface atoms.

For these nanoscale systems, where optical properties are governed by surfaces effects (especially metals and semiconductors), an adjustment of the constitutive parameters with size is essential to maintain the validity of the classical equations. This chapter presents a review of a theoretical model to correct the constitutive parameters with system size, focusing on outlining the physical principles involved in the interaction of electromagnetic waves with nanometric systems. In the different sections, we will show results of several research groups, including ours, about the behavior of the dielectric function in the UV-visible to near-IR (infrared) range appropriately corrected for few nanoscopic dimensions, as well as its applications to sizing for different 2D and 3D nanostructures. We will focus on studying dilute clusters of particles (average distance between particles of some wavelengths) with revolution symmetry such as nanospheres, nanowires, metallic core-shell spheres, and metallic nanotubes, where the thicknesses of the metal layers are of a few nanometers. In this way, the dielectric function will not only depend on the frequency of the electromagnetic wave but also on the characteristic dimensions of the nanoscale systems [16]. One of the main challenges at theoretical level is the correct description of the optical parameters of systems with nanometric scale. This parameterization of the dielectric function with the size allows describing the optical response of the system under study with a macroscopic quasi-classic model, based on Maxwell's equations.

In this study, there are two kinds of approaches: One is the top-down approach, in which the study of the nanostructures is reached from the bulk, and the other is the bottom-up approach, where the analysis starts from the atoms toward large clusters.

We analyze at this point, the behavior of the dielectric function for different sizes, starting from experimental bulk values toward smaller sizes up to subnanometric nanoparticles.

4   Experimental and Instrumental Methodology

4.1   Experimental Extinction Spectroscopy

Traditional methods for nanoparticle sizing are based on optical or electron microscopy. These methods have, in many cases, drawbacks concerning the preparation of

Fig. 5.1 Schematic for definition of extinction and scattering processes by an ensemble of particles

Incident wave

θ

Detector

Extinction

Scattered wave
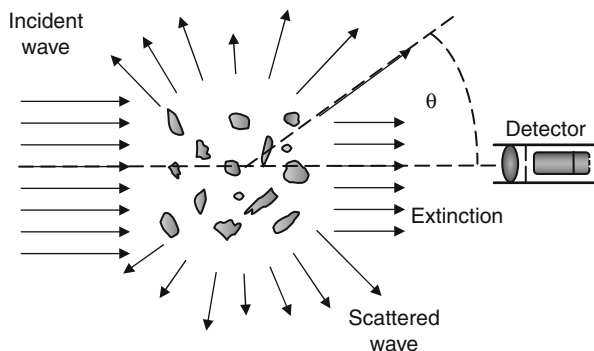
the sample or poor statistics. Optical spectroscopic techniques are often more suitable since measurements can be made without sample treatment, data acquisition can be very fast, they may be implemented for in situ analysis, and they are an excellent complement to electron microscopy.

Spectral extinction is one of these techniques which can be readily implemented using a commercial spectrophotometer. It is a very simple and suitable technique for sizing particles in the micron and submicron range, where it can be put in parallel with transmission electronic microscopy (TEM) and scanning electronic microscopy (SEM). Spectral extinction can be easily performed for dielectric [28, 29] and metallic nanoparticles [16, 25, 30–42] in diluted liquid suspensions. Figure 5.1 pictures a possible setup of the situation. When the detector is placed in the direction of the incident light, after the ensemble, it will measure an energy flux per unit area which is smaller than the power of the incoming wave.

Experimental results are fitted by Mie calculations (see Sect. 5.3.4) for spherical particles, where knowledge of the refractive index as a function of the wavelength for both the particle material and the solvent is necessary. For the metal dielectric function used in this Mie calculation, it is necessary to include the modifications for size for the free and bound electron contribution described in Sect. 5.1.

Spectrophotometers measure the extinction of light that is the fraction of light removed from the incident beam. Operatively, extinction can be derived from the relation given by the Lambert–Beer law:

$$I_t = I_i \exp\left(-\beta_{ext}\, l\right) \tag{5.1}$$

where I_i is the intensity incident over the sample, I_t is the transmitted irradiance, β_{ext} is the attenuation coefficient, and l is the length of the sample. When the dilution of the sample is such that the average interparticle distance in the medium is large enough so that incoherent scattering can be considered, it is possible to relate the attenuation coefficient of a sample of N particles per unit volume, with the single-particle cross section C_{ext}:

$$\beta_{ext} = N\, C_{ext} \tag{5.2}$$

When a set of measurements of I_t/I_i are performed over a range of wavelengths, the so-called extinction spectra is obtained. Results can be compared with the calculated spectral extinction efficiency, Q_{ext} (λ), for a given medium refractive index and for a given nanoparticle radius, which is used as fitting parameter. This spectral signature has information of the chemical composition of the sample as well as the size and distribution of sizes of the particles.

In general, samples consist of an ensemble of particles with a certain size distribution suspended in some liquid. To determine this distribution of radii, extinction measurements at a discrete set of wavelengths may be conducted, a method that is called multispectral extinction. Inversion of the experimental results should retrieve, in principle, the different radii values, although this is not a trivial task, since, in general, the scattering matrix is ill conditioned and a nonlinear inversion algorithm must be used to solve the problem.

For the case of large particles (compared with wavelength), when scattering is almost forward and the light can reach the detector, the measurement is not a pure extinction (scattering plus absorption) but an intermediate between absorption and extinction. Experimental results may be strongly altered unless special care is taken to avoid the unwanted forward-scattered light from reaching the detector. A small diameter pinhole placed at a suitable position between the sample and the detector will help enhance the reliability of the measurements. As the size of dielectric particles becomes smaller than the wavelength, the scattering spectrum smoothens its features and the spectral extinction technique loses gradually its power, thus making it an unsuitable method for measuring particles with mean radius below about 200 nm. However, it is interesting to notice that metal particles constitute one important exception to the rule mentioned above because their extinction spectra present clear size effects for radius well below the wavelength. For this reason, colloidal solutions of noble metals, like copper, gold, and silver, present intense color that is absent in bulk material. This behavior is due to surface modes, a class of electromagnetic modes that can couple light to particles in a very efficient way, as will be discussed in the next sections.

4.2 Experimental Fabrication and Fragmentation by Laser Ablation

The metal nanostructures which this chapter deals with were generated either by wet chemistry or by ultrashort pulse laser-based ablation methods. The former is extensively treated in the literature and will not be discussed here. The latter is centered in ablation of solid targets immersed in a cell with an appropriate liquid. Fabrication was performed focusing the laser beam over a sample of 1-cm diameter, which is placed over a PC controlled X-Y-Z translation stages with micrometer accuracy. The laser system was a Spectra Physics 100 fs pulse 800 nm wavelength Ti:Sa chirped amplified laser of 1 mJ pulse energy and 1 kHz repetition rate. After a few seconds of ablation, the liquid showed a typical coloring according to the ablated metal. Figure 5.2 shows the setup used to fabricate different metal Nps in solution with IR fs laser.
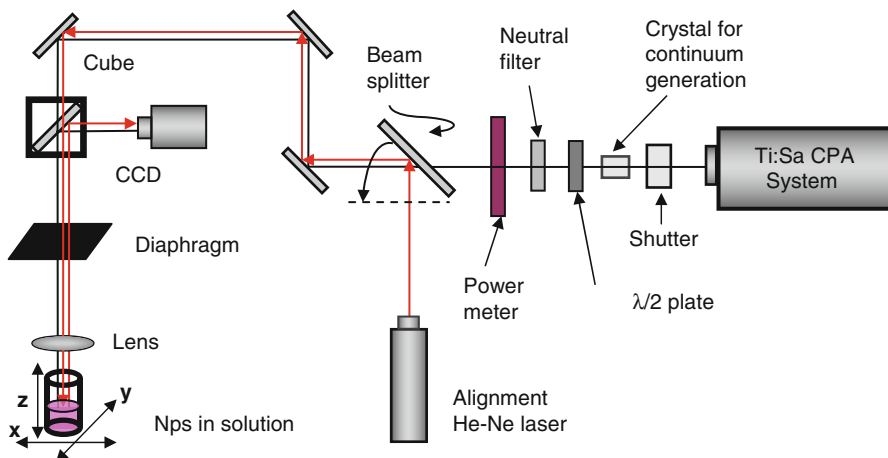
Fig. 5.2 Setup used to fabricate gold Nps in solution with IR fs laser and to perform fragmentation with SC generated using an external sapphire crystal

The second step consists in the fragmentation of the sample obtained before. This fragmentation process was carried out using two different sources of supercontinuum (SC) radiation: (1) SC produced by an external sapphire crystal and (2) SC produced by IR fs pulses in the same liquid solution. In both cases, radiation was applied to the solution during 30 min. This process enables to reach sizes of radius less than 2 nm. In the first case, the SC generated in the external sapphire crystal was focused on Nps solution to analyze the effect on size distribution after light interaction. A suitable IR cutoff filter could be inserted before the sample to filter out the 800-nm fundamental radiation [37, 38].

In the second case, fragmentation is carried out using the same setup, removing the sapphire crystal and the solid gold disk from the sample and leaving only the Nps solution. In this case, the IR radiation cannot be separated from the SC light generated in water. To characterize the size of gold Nps in water, optical extinction measurements in the 300–700 nm range by means of a commercial spectrophotometer were conducted.

5   Key Research Findings

5.1   About the Dielectric Functions of Metals

The optical parameters of metals determine many macroscopic characteristics such as shiny aspect and opacity to transmitted visible light. The reflection and transmission coefficients of light for different wavelength ranges may be described based on these optical parameters which, in turn, can be understood by assuming a simple model to characterize the microscopic structure of matter.

The electromagnetic response of matter is described by a frequency-dependent complex dielectric function, $\varepsilon(\omega) = \varepsilon'(\omega) + i\varepsilon''(\omega)$, which relates the value of the electric field $\vec{E}(\omega)$ with the displacement field $\vec{D}(\omega)$. The dielectric function for nanometric systems is not only a function of the wavelength (or frequency) of the incident radiation but also is sensitive to the size and shape of the particle [43–45]. As it was shown in the works of E. Coronado [43] and J. Kottmann [44], variations in the imaginary part of the dielectric function lead to dramatic changes in the optical response for nanoparticles and nanowires with asymmetric profiles.

The expression of the dielectric function for a nanoscopic particle is not trivial. Different approaches such as the jellium or quantum-chemistry models [16, 46, 47] may be used based on considerations related to electron collective behavior or in first principles calculations, respectively. However, if suitable and physically meaningful corrections are made, the classical concept of dielectric function can be extended down to nanometer sizes. This approach yields results that fit satisfactorily experimental data while giving physical insight about the electronic processes that give rise to macroscopic measurable parameters.

In general, this complex dielectric function for bulk metals can be decomposed into two terms, a complex free electron term and a complex interband (or bound electron) term. Since the dielectric function is additive [48], it can be written as:

$$\varepsilon(\omega) = \varepsilon_{free-electrons}(\omega) + \varepsilon_{bound-electrons}(\omega) = \varepsilon'(\omega) + i\varepsilon''(\omega)$$

So, real and imaginary parts of dielectric function have contributions from both complex free and bound electrons. In the following paragraphs, we will discuss briefly the separate contributions, introducing for each one an appropriate size dependence and will compare the results with available experimental data on real and imaginary parts of noble metal dielectric function. We will also analyze the influence of these size dependences on the optical extinction spectra of nanometric and subnanometric particles.

5.1.1 Free Electron Contribution

In order to model this response, a microscopic picture of matter is needed. One of the most basic models is the so-called Lorentz model, which assumes matter composed of electrons and ions as a collection of independent, identical, isotropic, and damped charged harmonic oscillators. So, optical properties are a consequence of the way in which these oscillators respond to electromagnetic fields.

For this model [49], the relative dielectric function ε defined as $\varepsilon = \in/\varepsilon_0$, corresponding to a collection of N damped harmonic oscillators per unit of volume, each with resonant frequency ω_0, can be written as:

$$\varepsilon = 1 + \frac{\omega_p^2}{\omega_0^2 - \omega^2 - i\gamma\omega}, \tag{5.3}$$

where $\omega_p^2 = N^* e^2/m\varepsilon_0$, e and m are the charge and mass of the electron, ε_0 is the permittivity of vacuum, and γ is the damping constant of the oscillators. For metals,

Fig. 5.3 Simplified electrons energy bands of solid metals
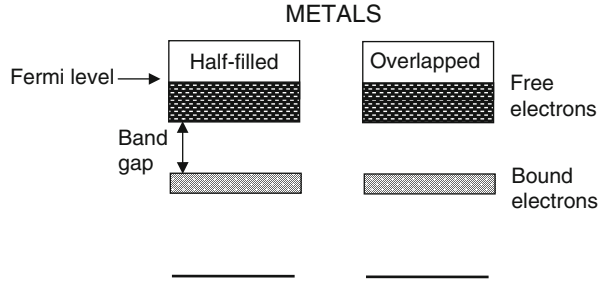
N^* is the density of free or conduction electrons that, in general, corresponds to one, two, or three electrons per atom.

Optical properties of materials are alternatively described by two sets of quantities: the real and imaginary parts of the complex refractive index, $N = n + ik$ or the real and imaginary parts of the dielectric function $\varepsilon = \varepsilon' + i\varepsilon''$. For nonmagnetic media, the relation $N = \sqrt{\varepsilon}$ holds. So, the real and imaginary parts of both parameters are related by:

$$\varepsilon' = n^2 - k^2, \tag{5.4}$$

$$\varepsilon'' = 2nk. \tag{5.5}$$

The energy states of electrons in solid materials may be represented by a nearly continuum energy levels grouped into different bands. For metals, the upper occupied band is partially filled with electrons or completely filled and overlapped with an upper empty band, as shown in a simplified form in Fig. 5.3.

Electrons in bulk metals are considered essentially "free" since they can be promoted to higher empty energy levels (from the top of the energy distribution, near the Fermi level) with very small photon energies. In this sense, it can be considered that they are not bound to the ion core, so their resonant frequency may be set equal to zero in the Lorentz model [50 (a, b)]. Therefore, the expression for the dielectric function of a "free electron metal" can be obtained according to the Drude Sommerfeld model, by putting $\omega_0 = 0$ in Eq. 5.3:

$$\varepsilon_{free}(\omega) = 1 - \frac{\omega_p^2}{\omega^2 + i\omega\,\gamma_{free}}, \tag{5.6}$$

with real and imaginary parts given by:

$$\varepsilon'_{free}(\omega) = 1 - \frac{\omega_p^2}{\omega^2 + \gamma_{free}^2}, \tag{5.7}$$

$$\varepsilon''_{free}(\omega) = \frac{\omega_p^2\,\gamma_{free}}{\omega\left(\omega^2 + \gamma_{free}^2\right)}. \tag{5.8}$$

The plasma frequency ω_p lies in the ultraviolet region of the spectrum and $\hbar\omega_p$ ranges from 4 to 20 eV. In the bulk metal, the damping constant γ_{free}, has a simple physical interpretation in terms of the average total time τ between collisions of free electrons with other electrons (electron–electron scattering), lattice vibrations (electron–phonon scattering), and imperfections. It can be expressed as:

$$\gamma_{free}^{bulk} = \frac{1}{\tau} = \frac{1}{\tau_{el-el}} + \frac{1}{\tau_{el-ph}} + \frac{1}{\tau_{im}} \qquad (5.9)$$

For nanoparticles smaller than the electron mean free path (a few tens of nanometers for bulk metals), scattering of electrons with the particle's boundaries (surfaces) becomes important. This process reduces the electron mean free path, which in turn leads to an increase in the imaginary part of the dielectric function. This has been evidenced experimentally for spherical particles [16, 51–54]. In these works, it is shown that for particle sizes below 10 nm, the resonance width becomes broader.

To account for this fact, it is necessary to include an additive term in Eq. 5.9 which must be inversely proportional to the average time between collisions of the electrons with the boundary of the particle, $\frac{1}{\tau_r} = C \frac{v_F}{r}$, where v_F is the velocity of the electrons at the Fermi level and r is the radius of the nanoparticle. The proportionality constant C accounts for the details of the electron scattering processes at the boundary and may be calculated from electrodynamic theory or quantum box model [55 (a–d)]. For spheres, its value ranges from 0.75 to 1.15 [51].

With these considerations, a size-dependent damping constant may be introduced and expressed as:

$$\gamma_{free}^{size} = \gamma_{free}^{bulk} + C \frac{v_F}{r} \qquad (5.10)$$

The second term of Eq. 5.10 becomes negligible for large radii r, and the size damping constant tends to the bulk value. When γ_{free} is replaced by the size-dependent expression of Eq. 5.10, Eqs. 5.7 and 5.8 take the form:

$$\varepsilon'_{free}(\omega, r) = 1 - \frac{\omega_p^2}{\omega^2 + \left(\gamma_{free}^{size}\right)^2} \qquad (5.11)$$

$$\varepsilon''_{free}(\omega, r) = \frac{\omega_p^2 \gamma_{free}^{size}}{\omega \left(\omega^2 + \left(\gamma_{free}^{size}\right)^2\right)} \qquad (5.12)$$

Using Eqs. 5.11 and 5.12, a set of curves for different radii values can be obtained for the real and imaginary parts of the dielectric function. Figure 5.4 shows an example for the case of gold (Au), when it is plotted against wavelength.
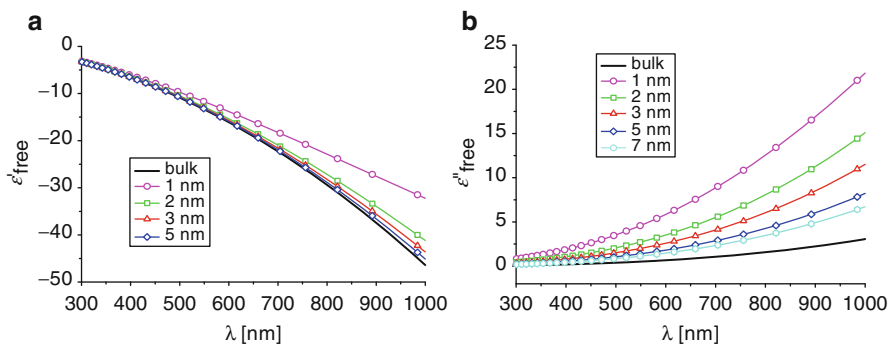
Fig. 5.4 Real (**a**) and imaginary (**b**) part of free electron contribution to the dielectric function for gold. Values used are: $C = 0.8$, $v_F = 14.1 \times 10^{14}$ nm/s Granqvist and Hunderi [56]

It can be seen that, as expected, each set of curves tends to a common wave-length-dependent curve (bulk) as the radius increases but presents clear differences for sizes between 1 and 10 nm, approximately, depending on the metal. It is clear then that it is possible to reproduce bulk values of the dielectric function by simply calculating Eqs. 5.11 and 5.12 for a radius close to 100 nm, since for these sizes, the second term in Eq. 5.10 is negligible. In this free electron approximation, all noble metals (Au, Ag, and Cu) behave alike and their dielectric functions are very similar, except for small differences arising from the different plasma frequency values.

5.1.2 Bound Electron Contribution (Bulk)

As it was mentioned at the beginning of Sect. 5.1, the complete expression for the complex dielectric function is made up by a free electron component and a bound electron component:

$$\varepsilon(\omega) = \varepsilon_{free}(\omega) + \varepsilon_{bound}(\omega) = \varepsilon'(\omega) + i\varepsilon''(\omega) \tag{5.13}$$

where $\varepsilon_{free}(\omega)$ can be made size-dependent through the Eqs. 5.11 and 5.12.

In a first approximation, the bound contribution may be considered non-size dependent. Its value may be determined from subtracting $\varepsilon_{free}(\omega)$ from the bulk experimental data $\varepsilon(\omega)$ taken from Palik or Johnson and Christy [57, 58] such as indicated in Eq. 5.13. For Nps with size smaller than 10 nm, the full complex dielectric function depends on size ($\varepsilon(\omega, r)$), and can be written as:

$$\varepsilon(\omega, r) = \varepsilon_{free}(\omega, r) + \varepsilon_{bound}(\omega) \tag{5.14}$$

where $\varepsilon_{free}(\omega, r)$ can be calculated by Eqs. 5.11 and 5.12.

Figures 5.5, 5.6, and 5.7 shows both the real and imaginary parts of dielectric function for Ag, Au, and Cu, respectively for bulk [58], and corrections for different radius of Nps calculated from Eq. 5.14.
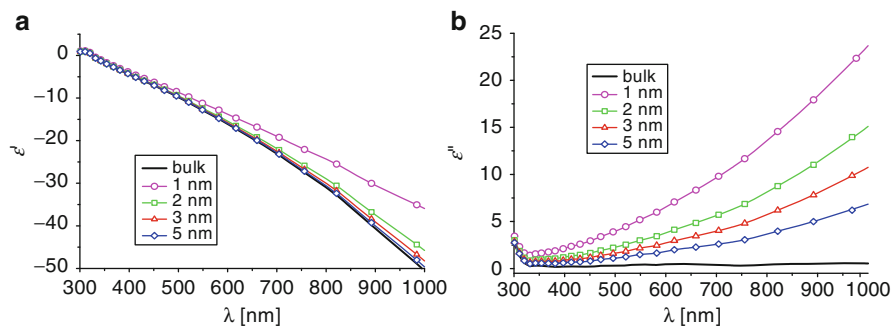
Fig. 5.5 Real (**a**) and imaginary part (**b**) for Ag dielectric function. In *black*, experimental bulk dielectric function [58]. In *color*, correction for a particle from 5 to 1 nm of radii [25]. See the panel for details
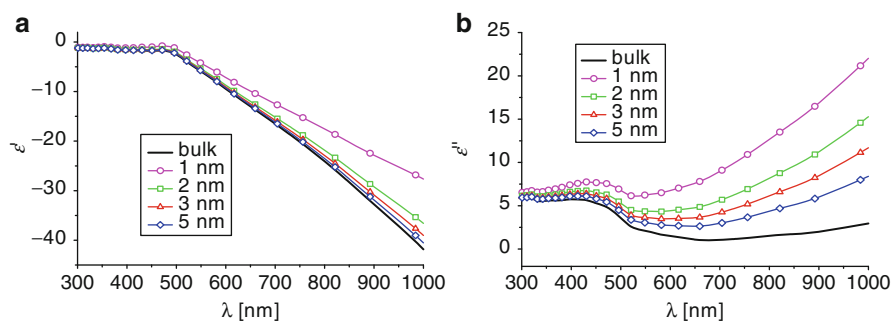

Fig. 5.6 Real (**a**) and imaginary part (**b**) for Au dielectric function. In *black*, experimental bulk values [58]. In *color*, correction for particles from 5 to 1 nm of radii [59]. See the panel for details

Fig. 5.7 Real (**a**) and imaginary part (**b**) for Cu dielectric function. In *black*, experimental bulk values [58]. In *color*, correction for particles from 5 to 1 nm of radii. See the panel for details
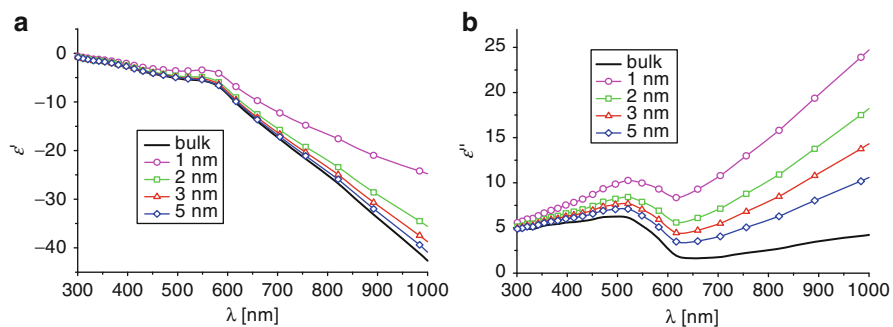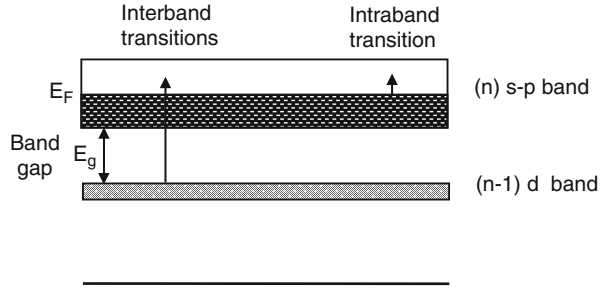
Fig. 5.8 Simplified electrons energy bands of noble metals

The real part shows an abrupt change of slope that is located at different wavelengths depending on the noble metal. The influence of bound electron is clearly associated for wavelengths smaller than the point of slope change. This is more dramatically evidenced in the behavior of the imaginary part, which shows a widened resonance at short wavelengths.

5.1.3   Bound Electron Contributions (Single Transition)

When the energy of the incoming photon is large enough to overcome the bandgap and promote valence (bound) electrons to the conduction band of the material, these electrons will add its contributions to the dielectric function. These kinds of transitions are called electronic interband transitions.

Figure 5.8 shows a simplified diagram for electrons energy bands of a noble metal at zero Kelvin. As s-p band is filled up to the Fermi energy, interband transitions can occur over a threshold energy value ($E_g + E_F$). Intraband transitions which correspond to free electrons can be excited with low energy photons.

The Drude model described above takes into account only electrons in the outer atomic orbitals (for example, 5s, 6s, and 4s states for silver, gold, and copper, respectively). However, interband transitions, such as the one from the 5d-band to the 6sp-band in gold, cannot be ignored when the incident light frequency falls in the visible region. This effect can be taken into account in $\epsilon^L_{bound}(\omega)$ by means of a standard Lorentz-like equation [4, 43, 61]:

$$\epsilon^L_{bound}(\omega) = 1 + \frac{{\omega'_p}^2}{\left(\omega_0^2 - \omega^2\right) - i\gamma_{bound}\,\omega} \qquad (5.15)$$

where ω'_p is introduced in analogy to the plasma frequency in the Drude model, γ_{bound} is the damping constant for the bound electron, and ω_0 is the resonance
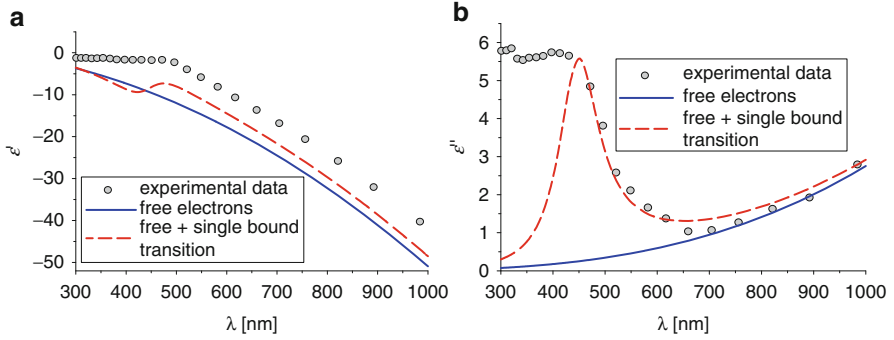
Fig. 5.9 Real (**a**) and imaginary (**b**) parts of the dielectric function for Au. *Open circles* correspond to the experimental bulk dielectric function from Johnson and Christy [58]. *Solid line*, free electron contribution for a bulk size; *dashed line*, free plus single bound electron contribution, also for a bulk size. Values used are: $\omega_0 = 4.19 \times 10^{15}$ Hz, $\omega'_p = 4.48 \times 10^{15}$ Hz and $\gamma_{\text{bound}} = 8.95 \times 10^{14}$ Hz [61]

frequency of the bound electron under the applied electric field. The real and imaginary parts are given by:

$$\varepsilon'^L_{bound}(\omega) = 1 + \frac{\omega'_p{}^2 \left(\omega_0^2 - \omega^2\right)}{\left(\omega_0^2 - \omega^2\right)^2 + \gamma_{bound}^2 \, \omega^2} \tag{5.16}$$

$$\varepsilon''^L_{bound}(\omega) = \frac{\omega'_p{}^2 \gamma_{bound} \, \omega}{\left(\omega_0^2 - \omega^2\right)^2 + \gamma_{bound}^2 \, \omega^2} \tag{5.17}$$

Since the dielectric function is additive, the complex expression can be written as:

$$\varepsilon(\omega, \, r) = \varepsilon_{free}(\omega, \, r) + \varepsilon^L_{bound}(\omega)$$

$$= 1 - \frac{\omega_p^2}{\omega^2 + i\omega \, \gamma_{free}^{size}(r)} + 1 + \frac{\omega'_p{}^2}{\left(\omega_0^2 - \omega^2\right) - i \, \gamma_{bound} \, \omega} \tag{5.18}$$

The total contribution of free and bound electrons to the dielectric function can be evaluated from Eq. 5.18.

In Fig. 5.9, we plot the real (a) and imaginary (b) parts of the dielectric function of gold in the visible and near-infrared range of the spectrum, using Eq. 5.18 with $r = 100$ nm to consider a bulk size. The bulk dielectric function, plotted as open circles, is calculated by interpolation using experimental data measured by Johnson and Christy [58]. Solid line corresponds to free electron contribution while dashed line represents the sum of intraband and a single interband transition [61]. Concerning the real part, some authors add an arbitrary constant term called ε_∞, whose value ranges between 1 and 10 and represents other interband transitions [61, 62], to fit the experimental data. For wavelengths $\lambda > 650$ nm, $\varepsilon(\omega, \, r)$ is

governed by its large negative real part. This is a consequence of the fast response of conduction electrons to the external electromagnetic excitation. This quasi-free behavior is like a shield causing a very fast damping of the EM fields within the metal.

Concerning the imaginary part, at wavelengths $\lambda < 600$ nm, the free plus single-transition bound electron model does not reproduce the experimental data. For this model, ε'' departs from the experimental data between 300 and 450 nm. Thus, with the inclusion of a single interband correction (Eq. 5.15), an agreement with the experimental curve is only obtained for 450 nm $<\lambda<$1,000 nm.

Similar general behavior (including the disagreements) was observed for the case of silver and copper, both for real and imaginary parts. So it is clear that a more complete model that considers explicitly other interband transitions is necessary to describe the complex expression of $\varepsilon(\omega, r)$.

5.1.4 Bound Electron Contributions (Multiple Transitions)

Since the single-transition bound electron contribution model fails for particles sizes comparable to the mean free path of conduction electrons, there is a need for an adequate description of the optical properties for large clusters formed by hundreds of atoms (molecule-like properties), which may help to have a better agreement between theory and experiment for short wavelengths. This is a topic under discussion since more than 50 years ago [63, 64]. In this section, we show a theoretical formalism to evaluate the interband contribution to the dielectric function. This contribution was estimated in last section based on a semiempirical analysis.

Pinchuk et al. [59] have analyzed the influence of interband electronic transitions on the frequency, amplitude, and bandwidth of the surface plasmon resonance in small metal nanoclusters. Their theoretical results for silver and gold, including the interband transitions in the model, lead to a more reasonable value for the plasmon bandwidth. A first approximation was based on the concept that the contribution due to interband transitions remains unchanged when material goes from bulk to small particles. Afterward, in the previous section, this fact was modified, specially for noble metals, considering transitions of bound electrons to conduction levels with a characteristic frequency ω_0.

Now we take a step forward, considering that for the contribution of bound electron transitions to the dielectric function in actual solids, ω_0 should be extended to cover all the allowed transitions to conduction band levels, as indicated in Fig. 5.10.

If the density of states on this band is represented by $D(\omega_0)$, the relative dielectric function corresponding to the bound electrons contribution can be written as:

$$\varepsilon_{bound}(\omega) = \int D(\omega_0)(1 - F)\, \varepsilon^L_{bound}(\omega, \omega_0)\, d\omega_0, \qquad (5.19)$$

Fig. 5.10 Schematic
diagram of energy levels for
gold, showing interband
transitions from d-state to
sp-states (*vertical arrows*).
DOS density of states
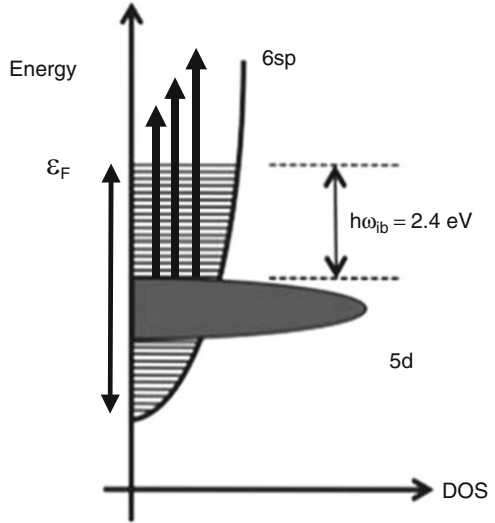
where F is the Fermi distribution, $(1-F)$ is the probability that the upper state is not
occupied, and $\varepsilon^L_{bound}(\omega, \omega_o)$ is the Lorentz dielectric function given by Eq. 5.15.
Rosei et al. [60] and Rosei [65] have given an explicit form for $D(\omega_0)$
corresponding to noble metals like gold and silver, and they show also the way to
calculate the limits of the integral in Eq. 5.19. Inouye et al. [66] have shown
a simplified expression of this calculation for gold assuming that the curvature of
the *d*-band can be ignored. In this case, the dielectric function can be written as:

$$\varepsilon_{bound}(\omega) = K_{bulk} \int_{\omega_g}^{\infty} \frac{\sqrt{x - \omega_g}}{x} [1 - F(x, T)]$$
$$\times \frac{(x^2 - \omega^2 + \gamma_b^2 + i \, 2 \, \omega \, \gamma_b)}{(x^2 - \omega^2 + \gamma_b^2)^2 + 4 \, \omega^2 \, \gamma_b^2} \, dx, \tag{5.20}$$

where $\hbar \omega_g$ is the gap energy (E_g); $F(x, E_F, T)$ is the Fermi energy distribution
function of conduction electron of energy $\hbar \, x$ at the temperature T with Fermi
energy E_F; γ_b represents the damping constant in the band to band transition; and
K_{bulk} is a proportionality factor. The reference for the energy is assumed at the top
of the *d*-band.

Figures 5.11 and 5.12 show calculated free electron (Eqs. 5.11, 5.12) and
multiple transitions bound electron contribution (Eq. 5.20) to the dielectric function
of gold and copper, respectively. The sum contribution (solid line) is compared with
experimental data given in Ref. [58] for bulk. Some parameters were taken from the
literature, while others were calculated previously by the authors [30]. These
parameters such as K_{bulk}, E_g, E_F, and γ_b produce different and independent effects
over the dielectric function.

Fig. 5.11 Calculated free electron and multiple transitions bound electron contribution to the dielectric function of gold. The sum contribution (*solid line*) is compared with experimental data given in Ref. [58] for bulk
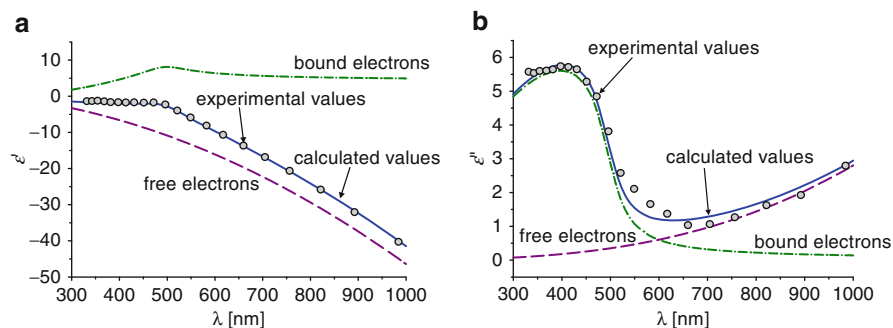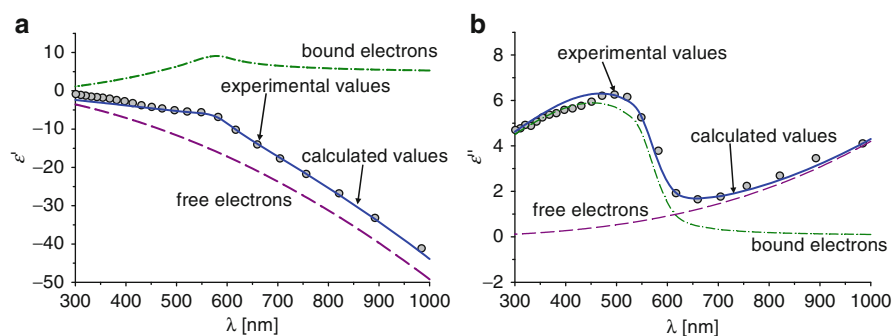

Fig. 5.12 Calculated free electron and multiple transitions bound electron contribution to the dielectric function of copper. The sum contribution (*solid line*) is compared with experimental data given in Ref. [58] for bulk

Fitting parameters and other relevant values for gold and copper are summarized in Table 5.1. It can be seen that with these parameters, the curves show excellent agreement with the experimental data without the need of adding an arbitrary constant.

For the contribution of bound electrons, no functional form is known to change the parameters in Eq. 5.20 as a function of the size of the particle. Some authors [16, 69, 70] introduced the idea that the electronic density of states is different for nanoparticles of different sizes. This fact affects Eq. 5.20 where part of the integrand is just the density of states in the upper band. Since small particles have larger spacing between electronic states, it is valid to conclude that the density of states will be smaller for very small Nps. It was proposed [16] to take account of this fact by changing the proportionality factor K_{bulk} in the contribution of bound electrons from its accepted bulk value to $K_{size} = K_{bulk}(1 - \exp(-R/R_0))$, where R is the radius of the particle and R_0 is a scale factor that represents the size for which the density of states can be considered to reach the value of the bulk.

Table 5.1 Optical parameters of bulk gold and copper

	Symbol	Value	Reference
Gold parameters			
Plasma frequency	ω_p	13×10^{15} Hz	Granqvist and Hunderi [56]
Damping constant for free electrons	γ_{bulk}	1.1×10^{14} Hz	Johnson and Christy [58]
Coefficient for bound electron contribution	K_{bulk}	2.3×10^{24}	Scaffardi and Tocho [30]
Gap energy	E_g	2.1 eV	Scaffardi and Tocho [30]
Fermi energy	E_F	2.5 eV	Scaffardi and Tocho [30]
Damping constant for bound electrons	γ_b	2.4×10^{14} Hz	Inouye et al. [66]
Copper parameters			
Plasma frequency	ω_p	13.4×10^{15} Hz	Cain and Shalaev [67]
Damping constant for free electrons	γ_{bulk}	1.45×10^{14} Hz	Johnson and Christy [58]
Coefficient for bound electron contribution	K_{bulk}	2×10^{24}	Santillán et al. [68]
Gap energy	E_g	1.95 eV	Santillán et al. [68]
Fermi energy	E_F	2.15 eV	Santillán et al. [68]
Damping constant for bound electrons	γ_b	1.15×10^{14} Hz	Santillán et al. [68]
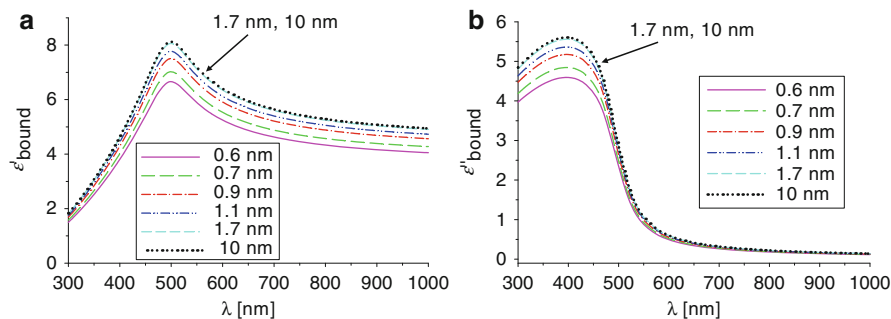
Fig. 5.13 Bound electron contribution to the dielectric function of gold, including correction for size. The correction is negligible for sizes close to 1.7 nm

Figures 5.13a, b show the spectral behavior of the real and imaginary parts of the bound electron contributions of gold for different nanometric and subnanometric sizes, using the Eq. 5.20 with the correction $K_{size} = K_{bulk}(1 - \exp(-R/R_0))$.

For the case of copper, Fig. 5.14a, b shows the spectral behavior of the real and imaginary parts of bound electron contribution for different subnanometric and nanometric sizes.

It can be observed from Figs. 5.13 and 5.14 that the curves corresponding to sizes larger than 2 nm are overlapped with each other. This is due to the fact that, for that size range, the correction included in the expression of K_{size} becomes negligible.
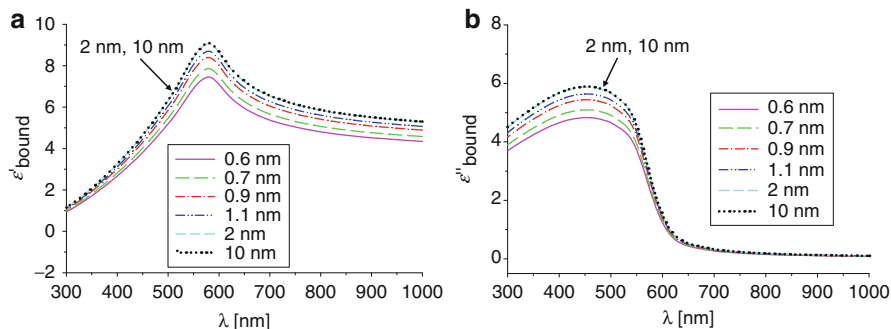
Fig. 5.14 Bound electron contribution to the dielectric function of copper, including correction for size. For sizes close to 2 nm, the correction is negligible

In the following section, we present results about the electromagnetic response of different nanometric systems. We show how changes in the dielectric function modify the optical properties of nanometric systems: metallic nanowires (2D scattering problem), nanotubes, spherical nanoparticles, and core-shell systems.

The different modification in the real and imaginary part of the dielectric function described above (arising from free and bound electron contribution) will be used in Sect. 5.3.4 to characterize experimentally the size of 3D spherical nanostructure from the features of their extinction spectrum.

5.2 Optical Extinction Spectroscopy

5.2.1 Nanoparticle Cross Section and Optical Theorem for Arbitrary Geometry

In this section, we outline the problem of the interaction of an electromagnetic wave with a nanometric sized particle [48, 71]. We use a rigorous 2D integral method based on Green's second identity and the extinction theorem for calculations of optical responses of arbitrary shaped particles. We then give a brief overview about the calculation of scattering and extinction cross section by small spherical particles following the method of Mie expansion, exploring the asymptotic behavior when the radius $a \to 0$.

Figure 5.15 shows the general problem of dispersion by a particle, considering that a polarized electromagnetic wave interacts with a particle of volume V with arbitrary geometry. The particle is characterized by a dielectric function $\varepsilon(\vec{r}) = \varepsilon'(\vec{r}) + i\,\varepsilon''(\vec{r})$.

Given the direction of incident electromagnetic field and the shape, size, and relative dielectric function $\varepsilon(\vec{r})$ of the scatterer, the goal is to determine the fields $\vec{E}(\vec{r})$ and $\vec{H}(\vec{r})$ at all points in space. The scatterer is assumed to be embedded in a homogeneous and isotropic lossless medium of dielectric constant ε_0. Electromagnetic fields must satisfy the macroscopic Maxwell's equations with the corresponding boundary condition on the particle [72]. In general, this is a complex problem that must be solved numerically, although analytical
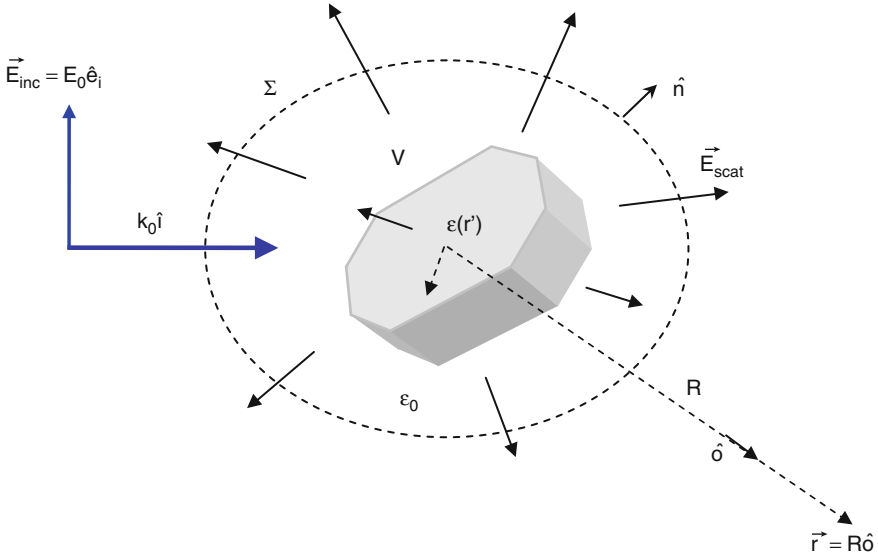
Fig. 5.15 Schematic for scattering calculation

expressions can be obtained for simple geometries or for certain approximations [58, 61, 73, 74].

In order to gain physical insight into the problem, we can write the total fields as a superposition of incident and scattered fields:

$$\vec{E} = \vec{E}_{inc} + \vec{E}_{scat}$$

$$\vec{H} = \vec{H}_{inc} + \vec{H}_{scat}$$

If we take a closed mathematical surface Σ containing the scatterer, the total energy flow per unit time and area that crosses this surface is given by the time-averaged Poynting vector $<\vec{\mathbf{S}}> = (1/2)\mathbf{Re}[\vec{\mathbf{E}} \times \vec{\mathbf{H}}^*]$, or

$$<\vec{S}> = <\vec{S}_i> + <\vec{S}_s> + <\vec{S}'> \tag{5.21}$$

It is interesting to note that the time-averaged Poynting vector for the total field can be written as a linear combination of energy flow per unit time for the incident field and scattered field plus a term that accounts for overlap of the fields:

$$<\vec{S}_i> = (1/2)\text{Re}[\bar{\mathbf{E}}_{inc} \times \vec{H}_{inc}^*], <\vec{S}_s> = (1/2)\text{Re}[\bar{\mathbf{E}}_{scat} \times \vec{H}_{scat}^*], \text{ and}$$
$$<\vec{S}'> = (1/2)\text{Re}[\bar{\mathbf{E}}_{inc} \times \vec{H}_{scat}^* + \bar{\mathbf{E}}_{scat} \times \vec{H}_{inc}^*].$$

By integrating Eq. 5.21 through the closed surface Σ, we find a simple relation for energy present in the system. The energy term corresponding to the incident field results in zero, since we assumed a lossless host medium. Thus, the energy balance for a metallic scatterer is given by:

$$- W_a = W_s + W',$$

where

$$W_s = \oint_{\Sigma} <\vec{S}_s> \cdot \hat{n} \, da, \quad W' = \oint_{\Sigma} (\vec{E}_{inc} \times \vec{H}^*_{scat} + \vec{E}_{scat} \times \vec{H}^*_{inc}) \cdot \hat{n} \, da \qquad (5.22)$$

W_a is the energy absorbed by the particle and $\hat{n}$ is the normal to the Σ surface.

The integral W', the total energy removed from the incident field by both scattering and absorption, can be written in an analytic form when the electromagnetic fields are considered in the far field.

We consider an incident electromagnetic wave with a wave vector $\vec{k}_0 = k_0 \hat{i}$ and electric field of the form:

$$\vec{E}_i = E_0 \hat{e}_i \, \exp[ik_0(\hat{i} \cdot \vec{r})]$$

The scattered waves, far from the scatterer, are considered spherical waves:

$$\vec{E}_{scat} = f(\hat{i}, \hat{o}) \, \frac{\exp[ik_0 \cdot \vec{r}]}{R}; \quad \vec{H}_{scat} = \sqrt{\varepsilon_0} \left[\hat{o} \times f(\hat{i}, \hat{o}) \right] \frac{\exp[i\vec{k}_0 \cdot \vec{r}]}{R}$$

where $f(\hat{i}, \hat{o})$ is the so-called scattering amplitude, which depends on the observation angle.

By substituting the incident and scattered field into Eq. 5.22 and integrating when $R \to \infty$, we obtain:

$$- W' = W_a + W_s = \frac{2\pi}{k_0} \sqrt{\varepsilon_0} \, \text{Im} \left[\hat{e}_i \cdot f(\hat{i}, \hat{i}) \right].$$

Absorption and scattering remove energy from the incoming electromagnetic field when light interacts with particles. At this point, we can introduce the extinction cross section C_{ext}:

$$C_{ext} = \frac{W_a + W_s}{|<\vec{S}_i>|} = \frac{4\pi}{k_0} \text{Im}[\hat{e}_i \cdot f(\hat{i}, \hat{i})] \qquad (5.23)$$

and

$$C_{scat} = \frac{W_s}{|<\vec{S}_i>|} = \int_{4\pi} |f(\hat{o}, \hat{i})|^2 d\Omega, \, C_{abs} = \frac{W_a}{|<\vec{S}_i>|} = \int_V k_0 \varepsilon''(\vec{r}') |\vec{E}(\vec{r}')| dV \quad (5.24)$$

Equation 5.21 is the so-called Optical Theorem or Forward Scattering Theorem [71, 75, 76], which is valid not only in electromagnetism but also in acoustics and quantum mechanics.

The electromagnetic problem reduces to find the scattering amplitude $f(\hat{o}, \hat{i})$. A simple analysis shows the dependence of $f(\hat{o}, \hat{i})$ with both the constitutive parameters and the shape of the nanoparticle. We first write Maxwell's equation in the following manner:

$$\vec{\nabla} \times \vec{E} = i\omega\mu_0\vec{H},$$

$$\vec{\nabla} \times \vec{H} = -i\omega\varepsilon_0\vec{E} + \vec{\xi}_e,$$

where $\vec{\xi}_e$ is consider like a source which generates the scattered waves and it is defined by [61]:

$$\vec{\xi}_e = \begin{cases} -i\omega\varepsilon_0[\varepsilon(\vec{r}) - 1]\,\vec{E} & in\ \ V \\ 0 & outside \end{cases}$$

If we write the scattered electromagnetic field as a function of the Hertz vector [62], we obtain:

$$\bar{E}_s(\vec{r}) = \vec{\nabla} \times \vec{\nabla} \times \vec{\Pi}_s(\vec{r}), \quad \vec{H}_s(\vec{r}) = -i\omega\varepsilon_0\vec{\nabla} \times \vec{\Pi}_s(\vec{r}), \tag{5.25}$$

where $\vec{\Pi}s(\vec{r}) = -\frac{1}{i\omega\varepsilon_0} \int\limits_V G_0(\vec{r}, \vec{r}')\xi_e(\vec{r}')\,dV'$.

$G_0(\vec{r}, \vec{r}')$ is the free space Green's function. In the far field, we can write $G_0(\vec{r}, \vec{r}')$ as (see Fig. 5.14):

$$G_0(\vec{r}, \vec{r}\,') = \frac{\exp[ik_0R - ik_0\,\vec{r}\,' \cdot \hat{o}]}{4\pi R}.$$

Then, substituting $G_0(\vec{r}, \vec{r}\,')$ for large R in to Eq. 5.25 we obtain:

$$\vec{E}_s(\vec{r}) = f(\hat{o}, \hat{i})\frac{\exp[ik_0R]}{R},$$

and

$$f(\hat{o}, \hat{i}) = \frac{k_0^2}{4\pi} \int_V \left\{-\hat{o} \times \left[\hat{o} \times \vec{E}(\vec{r}')\right]\right\}\left\{\varepsilon(\vec{r}') - 1\right\}\exp[-ik0\vec{r}\,' \cdot \hat{o}]dV' \tag{5.26}$$

The scattering amplitude $f(\hat{o}, \hat{i})$ depends on $\vec{E}(\vec{r}')$, the field inside the particle, and this magnitude is unknown in general. However, in many practical situations, it is possible to obtain a useful approximation to compute $f(\hat{o}, \hat{i})$.

From a theoretical point of view, for particles with radii much smaller than the wavelength, a quasi-static limit can be used. Under this quasi-static approximation, if we consider the scatterer with a spherical symmetry, the electromagnetic field inside the sphere is constant and proportional to the incident field [77]:

$$E(\vec{r}\,') = \frac{3}{\varepsilon + 2} E_o \hat{e}_i,$$

Substituting this expression in Eq. 5.26 and considering a uniform dielectric function for the scatterer, we obtain:

$$f(\hat{o}, \hat{i}) = \frac{k_0^2}{4\pi} 3\alpha_0 \, V \sin(\theta_{obs}),$$

where $\alpha_0 = \frac{\varepsilon - 1}{\varepsilon + 2}$ and $\sin(\theta_{obs}) = -\hat{o} \times (\hat{o} \times \hat{e}_i)$.

Under this approximation, both the scattering and absorption cross sections are given by:

$$Q_{scat} = \frac{C_{scat}}{\pi \, a^2} = \frac{8}{3}(k_0 a)^4 |\alpha_0|^2, \quad Q_{abs} = \frac{C_{abs}}{\pi a^2} = 4\, k_0 a \, \varepsilon'' \left| \frac{1}{\varepsilon + 2} \right|^2.$$

where a is the radius of the sphere.

A similar expression is obtained from an asymptotic Mie expansion (far field) for $ka \ll 1$, being a radii of the particle, as will be shown in Sect. 5.2.3.

For metallic particles, $\varepsilon' < 0$ at optical frequencies, so, the extinction cross section has a maximum when $\varepsilon' = -2$ for spheres and $\varepsilon' = -1$ for cylinders. This resonance is associated with collective oscillations of the free electrons at the metal induced by the incident electromagnetic fields. The physical region where the excitation into the metal occurs is given by the skin depth $\delta = \lambda \, / \, [4\pi \, \text{Im}[\sqrt{\varepsilon}\,]]$. These collective electronic oscillations at the surface of the metal are known as surface plasmon [78]. In contrast to flat interfaces (films, diffraction gratings, rough interfaces), in the case of a nanoparticle, the surface plasmon is confined to the three dimensions of the nanostructure and it is then called localized surface plasmon [78, 79]. In this situation, the localized surface plasmon resonance depends on the metal dielectric function and on the geometry of the nanostructure.

For cross sections with different geometry to the spherical or circular one, the analytical calculation is not easy even under the small-particle approximation. One approach to estimate the condition of resonance is a generalization given by $\mathbf{Re}(\varepsilon) = 1 - 1/\Gamma$, where Γ is a geometrical factor or effective depolarization factor which depends on the shape of the particle [14, 79]. However, Γ can also include some first order corrections to the quasi-static model such as the dynamic depolarization or the radiation damping. Γ takes the value 1/2 for circular cylinders and thus the resonance condition will be $\text{Re}(\varepsilon) = -1$. In first approximation, the Γ factor can be estimated from experimental curves for Q_{ext}. For ellipsoidal cross section, the value of Γ is related with the polarization of the incident wave: If the electric

field is along the major axis of the ellipsoid, Γ is smaller than 1/2, and if it is along the minor axis, Γ is greater than 1/2. Similar functional dependences are found for 3D nanowires [4, 14, 80].

The description of the scattering of electromagnetic waves by arbitrary nanosized obstacles has led to the development of several techniques to solve Maxwell's equations in inhomogeneous media. For example, the dipole discrete dipole approximation (DDA) [15, 81], finite difference methods in time domain (FDTD) [82, 83], multiple multipole expansion (MMP) techniques [84], transfer matrix methods [85, 86], or finite element methods in frequency domain [87] are among some of the most commonly used techniques to solve Maxwell's equations. All of them present advantages in certain aspects and disadvantages in others, but we will not go further into their description.

5.2.2 Scattering by Infinitely Long Wires

The method used to compute the scattered far field can deal with scattering problems of electromagnetic waves from systems formed by arbitrarily shaped bodies. Details of the general procedure can be found elsewhere [88–91]. In what follows we summarize the method applied to 2D systems with translations symmetry.

Let us consider a *s* or *p* incident polarized electromagnetic field with electric or magnetic vector $\vec{E}^{(inc)}(\vec{r}, t)$ or $\vec{H}^{(inc)}(\vec{r}, t)$, given by:

$$\vec{E}^{(inc)}(\vec{r}, t) = (0, \phi_s^{(inc)}(\vec{r}, \theta), 0) \exp[-i\omega t],$$

$$\vec{H}^{(inc)}(\vec{r}, t) = (0, \phi_p^{(inc)}(\vec{r}, \theta), 0) \exp[-i\omega t],$$

respectively. When these fields are incident upon a cylinder of cross section S limited by a curve C, and complex permittivity ε (Fig. 5.16), the expressions of the scattering field (per unit length) in each medium can be obtained using the extinction theorem for multiply connected scattering volumes [26]. The field is then represented in the form:

$$\phi_\alpha^{(0)}(\vec{r}, \theta) = \phi_\alpha^{(inc)}(\vec{r}, \theta) + \frac{i}{4} \int_{c^+} dl' \left[\frac{\partial G_0\left(\sqrt{\varepsilon_m} k_0 |\vec{r} - \vec{r}'|\right)}{\partial \hat{n}'} \phi_\alpha^{(0)}(\vec{r}', \theta) \right.$$

$$\left. - G_0(\sqrt{\varepsilon_m} k_0 |\vec{r} - \vec{r}'|) \frac{\partial \phi_\alpha^{(0)}(\vec{r}', \theta)}{\partial \hat{n}'} \right], \ if \ \vec{r} \in host\ medium$$

$$\phi_\alpha^{(0)}(\vec{r}, \theta) = 0, \quad if\ \vec{r} \notin host\ medium \tag{5.27}$$

$$\phi_\alpha^{(1)}(\vec{r}, \theta) = -\frac{i}{4} \int_{c^-} dl' \left[\frac{\partial G_1(\sqrt{\varepsilon} k_0 |\vec{r} - \vec{r}'|)}{\partial \hat{n}'} \phi_\alpha^{(1)}(\vec{r}', \theta) - G_1(\sqrt{\varepsilon} k_0 |\vec{r} - \vec{r}'|) \frac{\partial \phi_\alpha^{(1)}(\vec{r}', \theta)}{\partial \hat{n}'} \right], \quad if\ \vec{r} \in S$$

$$\phi_\alpha^{(1)}(\vec{r}, \theta) = 0, if\ \vec{r} \notin S.$$

$$\tag{5.28}$$

Fig. 5.16 Schematic for scattering calculation for infinitely long wires
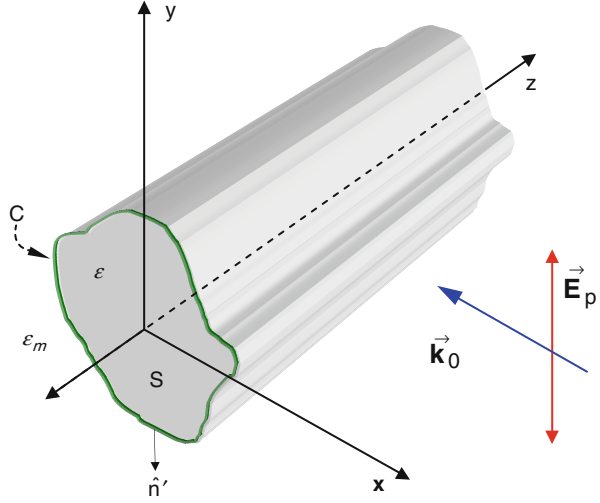
α denotes *s*- or *p*-polarization, and $\phi_\alpha^{(j)}(\vec{r}, \theta)$, with $j = 0, 1$, represents the complex amplitudes in the host medium (ε_m) and inside the cylinder, respectively. In a 2D configuration, the Green's functions are $G_j(\sqrt{\varepsilon_j}k_0|\vec{r} - \vec{r}'|) = i\pi H_0^{(1)}(\sqrt{\varepsilon_j}k_0|r - r'|)$, where $H_o^{(1)}$ are the zero-order, first class, Hankel functions and dl' is the differential element of line along the C contour. The symbol c^+ denotes that the integration variable $\vec{r}'$ tends to the contour C from outside of surface S (the normal $\hat{n}'$ points outward of surface S) and c^- denotes that the integration variable $\vec{r}'$ tends to the contour C from inside of surface S (the normal $\hat{n}'$ points inward of surface S). The electromagnetic field expressions for the far zone can be obtained from the previous equations making use of the asymptotic expressions for the Hankel functions for $|\vec{r} - \vec{r}'| \to \infty$, and the boundary conditions:

$$\phi_\alpha^{(0)}(\vec{r})\Big|_{\vec{r} \in c^+} = \phi_\alpha^{(1)}(\vec{r})\Big|_{\vec{r} \in c^-}, \quad \frac{\partial \phi_\alpha^{(0)}(\vec{r})}{\partial \hat{n}'}\Big|_{\vec{r} \in c^+} = \eta_\alpha \frac{\partial \phi_\alpha^{(1)}(\vec{r})}{\partial \hat{n}'}\Big|_{\vec{r} \in c^-},$$

where $\eta_p = \dfrac{\varepsilon_m}{\varepsilon}$ and $\eta_s = 1$.

In particular, the transmitted far field takes the form:

$$\phi_\alpha^{(t)}(r, \theta) = \sqrt{\frac{2}{\pi\sqrt{\varepsilon_m}k_0 r}} \exp\left[i\sqrt{\sqrt{\varepsilon_m}k_0 r} - \pi 3/4\right] T(\theta), \qquad (5.29)$$

where

$$T(\theta) = \frac{i}{4} \oint_{c^+} \left[\left(\hat{n}' \cdot \vec{k}_t\right)\phi_\alpha^{(0)}(\vec{r}') - i\frac{\partial \phi_\alpha^{(0)}(\vec{r}')}{\partial \hat{n}'}\right] \exp(-i\vec{k}_t \cdot \vec{r}')\, ds', \qquad (5.30)$$

is called the amplitude function of the scattering of the cylinder [56], and $\vec{k_t}$ is the propagation vector of the scattered wave, defined by,

$$\vec{k_t} = k_0 \sqrt{\varepsilon_m} \, (\sin\theta_t, 0, \cos\theta_t). \tag{5.31}$$

A Gaussian incident beam of half-width W was considered. With this kind of beams, we can simulate a plane wave by setting W sufficiently large [25].

The optical properties of the cylinder material are introduced only through the frequency-dependent dielectric functions ε and ε_m that was used in Eqs. 5.27 and 5.28. Once the far field is calculated, the extinction cross section per unit length Q_{ext}, can be determined by using the optical theorem [48, 71, 76]:

$$Q_{ext} = C_{ext}/2a = \frac{2}{x}\text{Re}[T(0)], \tag{5.32}$$

where $x = k_0\,a$ is the size parameter of the cylinder. Calculated Q_{ext} would be compared with experimental extinction spectra.

The method described here was extended to consider more complex systems such as nanotubes and coated wires [92].

5.2.3 Scattering by Spheres

This section is devoted to calculate 3D scattering for different structures such as bare-core or core-shell spherical nanoparticles. For calculations of cross sections, in this section, we resume the basic concepts involved in Mie Theory [48].

If a single spherical particle of radius a is considered, we can write the extinction cross sections (Eq. 5.23) in terms of the Mie [48] expansion coefficients a_n and b_n as:

$$C_{ext} = \frac{W_a + W_s}{\left|<\vec{S_i}>\right|} = \frac{2\,\pi}{k^2} \sum_{n=1}^{\infty} (2n+1) \; \text{Re} \, (a_n + b_n) \tag{5.33}$$

where

$$a_n = \frac{\mu \, m^2 j_n(mx) \, [x j_n(x)]' - \mu_1 j_n(x) \, [m x j_n(mx)]'}{\mu \, m^2 j_n(mx) \left[x \, h_n^{(1)}(x)\right]' - \mu_1 h_n^{(1)}(x) \, [m \, x j_n(mx)]'} \tag{5.34}$$

$$b_n = \frac{\mu_1 j_n(mx) \, [x j_n(x)]' - \mu_1 j_n(x) \, [m x j_n(mx)]'}{\mu_1 j_n(mx) \left[x' h_n^{(1)}(x)\right]' - \mu_1 h_n^{(1)}(x) \, [m x j_n(mx)]'} \tag{5.35}$$

and the primes indicating derivatives with respect to the argument of the function; μ and μ_1 are the magnetic permeabilities of the surrounding medium and of

the spherical particle, respectively; $x = 2 \pi N a / \lambda$ is the called *size parameter* with $N = \sqrt{\varepsilon_m}$ being the refractive index of the medium; $m = N_1 / N$ is the relative refractive index. Finally, j_n and h_n are the spherical Bessel and Hankel functions, respectively.

If the size of the sphere is small compared with the incident wavelength, only the first two terms on the expansion are relevant (dipolar term). With the asymptotic form for a_1 and b_1 and considering the lowest order in x [48], the expressions for absorption and scattering efficiency factors Q are:

$$Q_{abs} = 4 \, x \, \mathrm{Im} \left(\frac{\varepsilon_1 - \varepsilon_m}{\varepsilon_1 + 2\varepsilon_m} \right) \tag{5.36}$$

$$Q_{sca} = \frac{8}{3} \, x^4 \, \left| \frac{\varepsilon_1 - \varepsilon_m}{\varepsilon_1 + 2\varepsilon_m} \right|^2 \tag{5.37}$$

These expressions are identical to that obtained from the electrostatic approximation using the Optical Theorem.

If scattering is small compared with absorption, the absorption cross section may be expressed as:

$$C_{abs} = k \, \mathrm{Im}(\alpha) \tag{5.38}$$

where $k = \frac{2 \pi N}{\lambda}$ is the wavenumber in the medium surrounding the particle, λ is the wavelength of the incident light in vacuum, and α is the polarizability given by:

$$\alpha = 4 \, \pi \, a^3 \alpha_0 \tag{5.39}$$

For more complex structures, like core-shell spherical Nps, the expression of the polarizability is [48]:

$$\alpha = 4 \pi R_2^3 \, \frac{(\varepsilon_2 - \varepsilon_m) \, (\varepsilon_1 + 2\, \varepsilon_2) + f \, (\varepsilon_1 - \varepsilon_2) \, (\varepsilon_m + 2\, \varepsilon_2)}{(\varepsilon_2 + 2\, \varepsilon_m) \, (\varepsilon_1 + 2\, \varepsilon_2) + f \, (2\, \varepsilon_2 - 2\, \varepsilon_m) \, (\varepsilon_1 - \varepsilon_2)} \tag{5.40}$$

where $f = \left(\frac{R_1}{R_2} \right)^3$ is the ratio between inner and outer radius volumes; $R_1 = R_{core}$ is the metal central core; $R_2 = R_{core+coating}$ is the outer radius (metal core + shell); and $\varepsilon_1 = \varepsilon_1(\lambda, \, R_1)$, $\varepsilon_2 = \varepsilon_2(\lambda, \, R_2 - R_1)$, and ε_m are the dielectric functions of the core, coating (shell), and surrounding medium, respectively. When the metal dielectric function in the above expressions is modified by size according to Eqs. 5.11, 5.12, and 5.20, it is possible to calculate the extinction cross section for sizing small nanoparticles according to Eq. 5.38. This procedure will be used in Sect. 5.3.4 to fit experimental extinction spectra results in the visible-NIR range for bare-core and core-shell nanoparticles.

5.3   Theoretical and Experimental Results

In this section, we review some relevant results from the literature for the optical response of nanoscale systems. We show theoretical and experimental results of physical observables in the far field (optical cross sections) and how these observables depend on both the size and shape of the nanoparticle.

In recent years, great interest has developed in the study of nanoscale systems, from the synthesis and manufacture of nanoparticles, characterization and optical response up to their manipulation and physical properties control. Different areas of knowledge (chemistry, biology, physics, etc.) are making a significant amount of contributions to the subject. This is evidenced by the large number of interdisciplinary citations in recent reviews on the topics (see for instance Refs. [1, 2, 4, 7, 93–95]).

The optical properties of noble metals – in particular the structures of silver, gold, copper, aluminum, titanium – can be manipulated by appropriate engineering of nanoparticles (or nanostructures) and this subject is its main attraction. Understanding the optical response of nanoscale systems promote a variety of potential applications ranging from simple interaction molecules, optical crystals and photonic metamaterials. For instance, in surface-enhanced Raman spectroscopy [96–101], chemical and biological sensors have been proposed based on plasmon resonant particles [1, 102–104]. For scanning near-field optical microscopy, metallic particles provide large, yet well-localized near-field sources [105–113], and can therefore increase the resolution.

Small silver or gold particles and wires are also highly interesting for optical devices, as they provide efficient, frequency-selective scatters with sub-wavelength dimensions, allowing further device miniaturization. Moreover, silver and gold nanowires can guide electromagnetic modes over several microns [8, 114–118], coupled plasmon resonant nanoparticles can be used for evanescent optical transport [119–124], and nanoholes in metal films allow the filtering of optical signals [125–127]. Most recently, an active optical component, similar to a transistor, was proposed using the local field amplification associated with the excitation of plasmon resonances [12, 128] or the ablation of cancer cells in vivo [2, 7, 93, 94].

In general, numerical computations are necessary to understand the optical properties of arbitrarily shaped plasmon resonant particles in detail. In particular, the knowledge of the complex relationship between shape and size of the particles and its plasmon resonance spectrum allows designing nanoparticles for specific applications. This knowledge is required both for individual and interacting metal nanoparticles.

5.3.1   Electromagnetic Responses of Infinitely Long Nanowires: A 2D Scattering Problem

In this subsection, we deal with nanometric systems with translational symmetry. In particular, we show the electromagnetic response of metallic infinitely long nanowires and metallic nanotubes (2D metal dielectric core-shell systems). The solution of 2D problems allows qualitative and quantitative studies of the physical phenomena involved in electromagnetic interaction, without loss of generality.

As we mentioned in Sect. 5.2.1, the electron collective oscillation occurs within a narrow strip from the particle surface. The rapid response of free electrons in metals to external fields is the cause of the rapid damping of electromagnetic fields inside the metal giving rise to the skin effect. It is interesting to note that, for Ag particles, the skin effect depth is about 6–10 nm around the resonance frequency. Therefore, when the electromagnetic field falls on nanoparticles ($a < 10$ nm), the electromagnetic resonances related to the plasmon excitation practically occur in the volume of the particle. Due to these characteristics, we will call these resonances "eigenmodes of the system" which are a solution of the homogeneous problem.

The small metallic particle shows a complete polarization and the free electrons are confined to oscillate within its volume. Thus, the optical properties for these systems are substantially modified respect to larger ones. This behavior with size affects the constitutive parameters of the nanoparticle, as was shown in the Sect. 5.1.1

5.3.2 Nanowires

In Figs. 5.5, 5.6, and 5.7 (Sect. 5.1), we have shown results of applying the correction by size to Ag, Au, and Cu dielectric functions for particles with radii less than 7 nm. For infinitely long nanowires, a new condition is established: The permittivity depends on the polarization state of the illuminating wave. Two different dielectric functions may be defined: $\varepsilon(\omega)$ corresponding to silver bulk for s-waves (or TM), and $\varepsilon(\omega,r)$ for p-waves (or TE), where the size correction is included [25]. For this configuration, only p-waves show eigenmode resonances.

By inspection of the dielectric functions, we can see a clear increase of slope in the imaginary part as the particle radius decreases, while the real part displays much less variation, with a tendency to decrease its slope. This behavior of the dielectric constant (which is only corrected by size) is reflected in the cross section of extinction.

In Fig. 5.17, we show the evolution of the extinction cross section (p-waves) with the incident wavelength for different Ag and Au nanowires. The position of the resonant peak exhibits a clear dependence on the size. As the particle radius decreases, the resonant peak maximum is blueshifted.

This effect is particularly notorious for Ag nanowires (Fig. 5.17a). In Fig. 5.17b, we plot the peak position (resonant wavelength) depending on the radius, which clearly shows this blueshift. In the Fig. 5.17b too, we compare the same system but when it is immersed in index matching oil (refractive index approximately 1.52 at 500 nm). By comparing the peaks curve, we can see the redshifts of all resonance spectra due to change in the refractive index of the surrounding medium.

For the Au nanowires, the blueshift is less noticeable and for wires with radii less than 7 nm, the peak displacement is within the numerical error (see Fig. 5.17c). With respect to the displacement of the peaks with the particle size, there is not total agreement today. In the review of Link et al. [129], the authors devote a paragraph to comment about the disagreement in resonant peak shift. In the literature both redshifts and blueshifts of the peaks are reported. Recently, we can observe that this
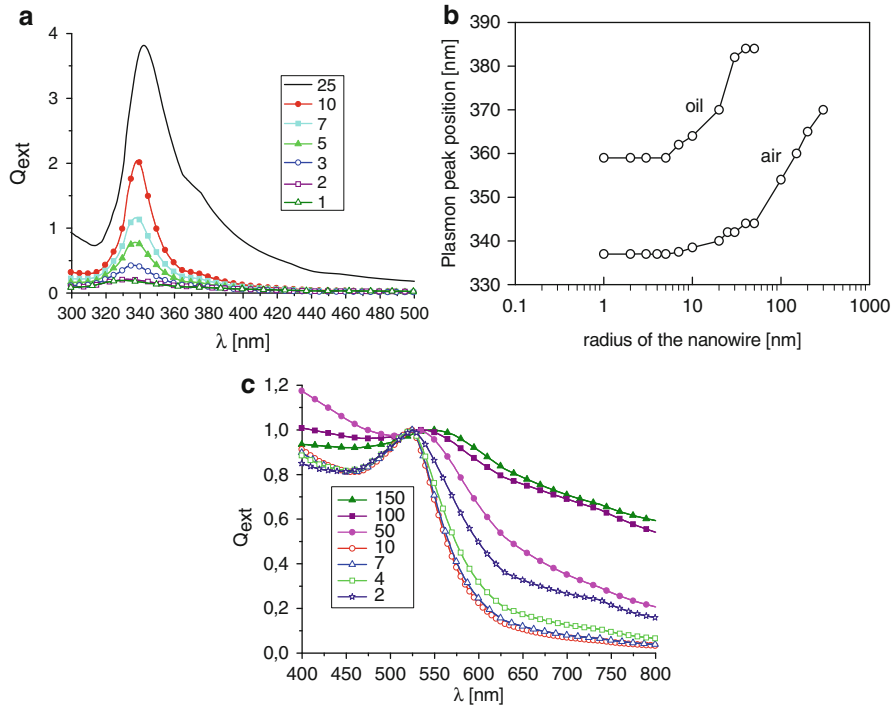
Fig. 5.17 (**a**) Behavior of Q_{ext} for p-polarized illumination with the wavelength for Ag nanowires with different radii. (**b**) Evolution of the resonant peak position with the radius. (**c**) Idem to (**a**) but Au nanowire normalized to the height of the resonance peak. In both cases, a blueshift is observed when the radius of the nanowire is reduced. Resonance peak position versus the radius of the silver nanowire for different host media: air and index matching oil

different behavior is produced by a nanoscopic shell due to the fabrication presses: oxide metal shell (i.e., in Ag nanoparticles) [130], surface modified in chemical process (i.e., in Au nanoparticles), etc.

In all cases studied, we observe a similar optical response: The position of the resonance peak does not change substantially with decreasing radius (less than 5 nm) and neither does the real part of the dielectric constant. As the radius decreases, the resonance peak broadens and decreases in height, while the imaginary part of the dielectric constant increases.

Another way, for s-waves, no eigenmode excitations are possible for 2D nanowires, but a clear difference in the spectra corresponding to different radii can be observed. In Fig. 5.18, we show the evolution for the extinction cross section with the wavelength for the incident s-wave. For radius larger than 10 nm, the contrast (relative difference between the maxima and the minima of the extinction cross section) between the ridge at 260–275 nm and the dip at 320–330 nm can be used to characterize the radii of the cylinders.
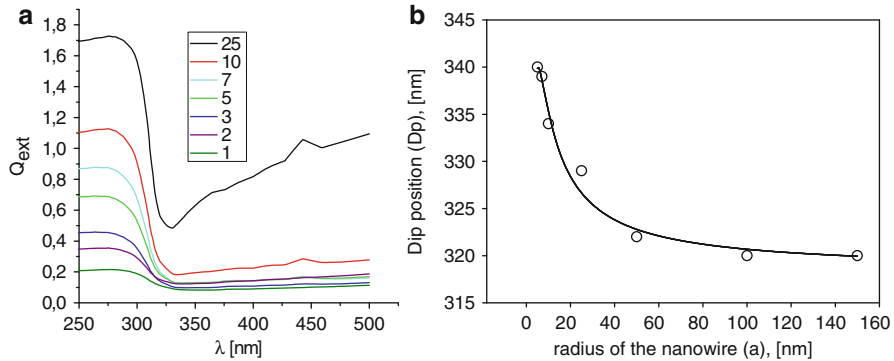
Fig. 5.18 (**a**) Evolution of Q_{ext} for s-polarized illumination as a function of wavelength for Au nanowires with different radii. (**b**) Evolution of the resonant peak position with the radius in air
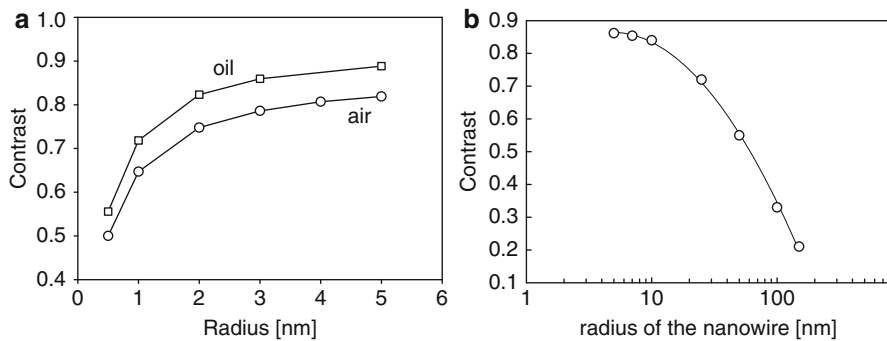

Fig. 5.19 Contrast curves as a function of Ag nanowire radius. (**a**) p-polarization for two host media, oil and air. (**b**) s-polarization in air

In Refs. [16, 25, 53], it has been proposed a useful tool based on contrast measurements. In Fig. 5.19, we show the contrast curves for characterizing the size of nanowires.

These qualitative optical properties are observed in 2D and 3D systems. The electromagnetic responses of metallic nanoparticles are not only sensitive to size of the particles, but also are sensitive to both the surrounding environment as well as its shape [74, 129].

In particular, the resonant frequencies of eigenmodes are sensitive to the geometry of the particles. The main attraction of the nanoparticles design is the possibility of tuning the resonant excitation of eigenmodes in a wide bandwidth, allowing a large number of applications, from the design of optical nanoantennas [123, 131], construction of plasmons waveguide of some nanometers wide [62, 121], development of more efficient solar cells, or the possibility of applying these resonant systems in detecting and/or destruction of cancer cells (photothermal therapy) [93].
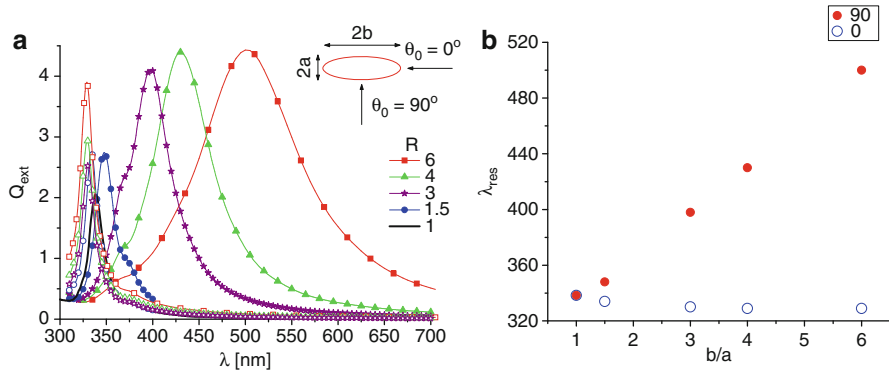
Fig. 5.20 Optical response for Ag nanowires with elliptic cross section and different aspect ratios. (**a**) Evolution of the extinction cross section Q_{ext} with wavelength for two different incident p-illumination modes: electric field parallel to major axis b ($\theta_0 = 90°$) – *solid symbols*; electric field parallel to the minor axis a ($\theta_0 = 0°$) – *hollow symbols*. (**b**) Evolution of the maximum of resonance peak as a function of the aspect ratio for both incidences. See the *insets* in panels (**a**) and (**b**)

A slight deviation from circular (spherical) geometry produces a splitting of the lower energy peak. This effect is noticeably for Ag particles, where eigenmode resonance shows a single well-defined peak for circular geometry (see Fig. 5.17a).

In Fig. 5.19, we show normalized extinction curves (respect to the geometrical shadow) as a function of wavelength for Ag nanoparticles with different aspect ratios (relationships between major and minor axes) **R** = b/a: from **R** = 1 (a = b = 10 nm) up to **R** = 6 (a = 10 nm, b = 60 nm). As we can see in Fig. 5.19, two branches (channels) are opened which depend on the polarization of the incident wave. One of them, when the peak position shifts to shorter wavelengths, corresponds to the electric field parallel to the minor axis – open symbols – (incidence to 0°, see the inset in Fig. 5.20a) and the other one is redshifted when the electric field is along the major axis – solid symbol – (incidence to 90°).

In Fig. 5.20b, we show the evolution of the resonance peak versus the aspect ratio **R** = a/b. The behavior of the resonant wavelengths is quasi-linear with **R**. With blue hollow circles, we show the evolution of resonance blueshifted peaks and with solid red circles, the redshifted peak ones. Because the minor axis is constant, the blueshift is not very pronounced, $\Delta\lambda = 9.4$ nm with respect to the perfect circle **R** = 1.

A similar behavior is observed for Au nanowires with elliptical cross section. In Fig. 5.21, we show the evolution of the extinction cross section for identical geometrical parameters to Fig. 5.20.

A qualitative explanation of the optical response for particles with volume (surface) ellipsoidal can be given under the non-retarded field hypothesis. This theory is based on an electrostatic solution for the principal values of the polarizability tensor, α_j, with a relative complex dielectric function $\varepsilon(\lambda)$ [48].
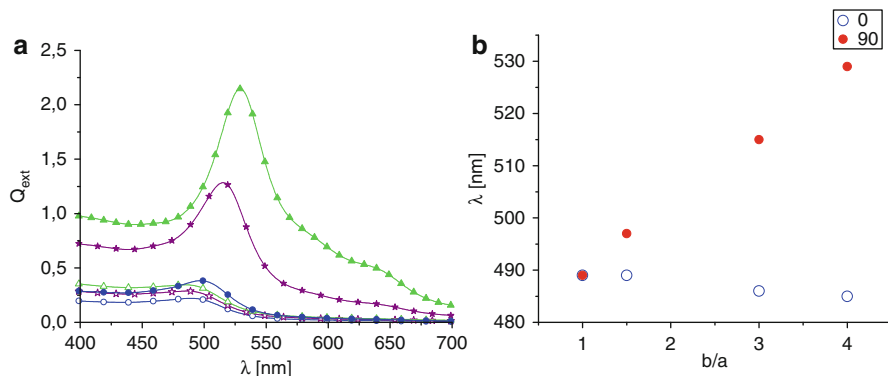
Fig. 5.21 Optical response for Au nanowires with elliptic cross section and different aspect ratios. (**a**) Evolution of the extinction cross section Q_{ext} with wavelength for two different incident p-illumination modes: electric field parallel to major axis b ($\theta_0 = 90°$) – *solid symbols*; electric field parallel to the minor axis a ($\theta_0 = 0°$) – *hollow symbols*. (**b**) Evolution of the maximum of resonance peak as a function of the aspect ratio for both incidences. See the *insets* in panels (**a**) and (**b**)

$$\alpha_j = 3V \frac{\varepsilon - 1}{3 + 3\Gamma_j(\varepsilon - 1)}, \tag{5.41}$$

V is the ellipsoidal volume and Γ_j are the geometrical depolarization factors. When the three axis of the ellipsoid are equal, the geometrical factor is degenerated and equals to 1/3 (or 1/2 for 2D problem). For small Rayleigh particles, the light-scattering contribution to the total extinction is usually neglected, so optical absorbance Q_{abs} is calculated through the absorption cross section averaged over random orientations of spheroids. Most papers on the optical properties of metal nanoparticles suspensions used the classic Gans theory. The qualitative behavior shown in Figs. 5.19 and 5.20 was observed experimentally in Au nanorods [13, 19].

Another way to control the frequency of excitation of eigenmodes in nanoparticles is through core-shell systems: dielectric particles coated with metal shell. In this case, controlling the thickness of the metal layer and the dielectric particle size is possible to tune the proper mode at determined frequency.

In the next section, we describe the optical response of metallic nanotubes. That is, hollow tubes with nanometric metallic walls and dielectric cylinders coated with a metallic layer.

5.3.3 Nanotubes

Geometrically, the nanotubes are formed by two coaxial cylinders forming an annular surface (wall of the nanotube) which is considered metallic. When the core of the nanotube is filled with a dielectric material, it is the 2D equivalent problem to the core-shell 3D system [42].

As it was shown for a single particle, the study of these 2D systems provides all the information necessary to understand the physical mechanisms involved in three-dimensional problems.
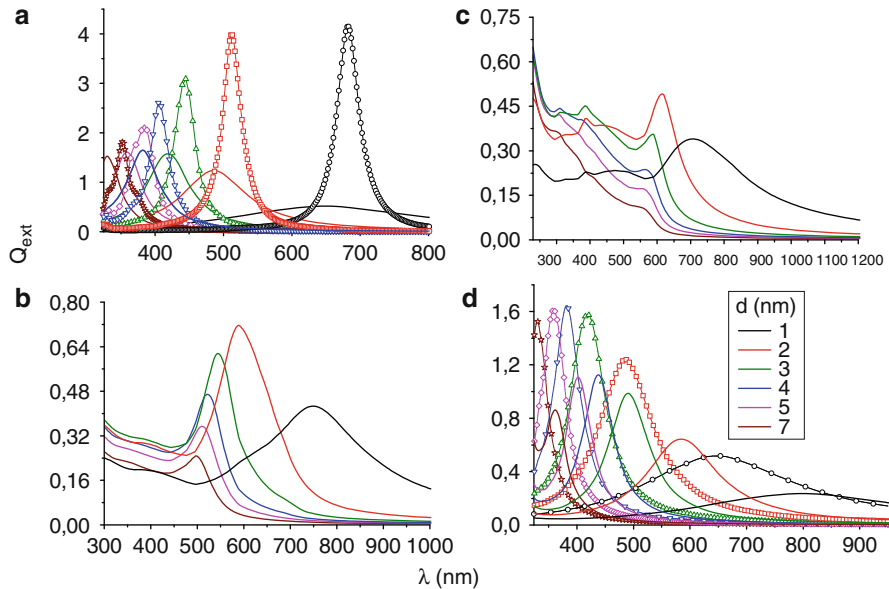
Fig. 5.22 Behavior of Q_{ext} as a function of the incident wavelength for different metallic nanotubes. (**a**) Ag nanotubes: in *solid line* Q_{ext} when the dielectric function is corrected by the thickness of the metallic shell and *hollow symbols* Q_{ext} for bulk dielectric function; (**b**) Q_{ext} for Au nanotubes; (**c**) idem to (**b**) for Cu nanotubes and (**d**) Q_{ext} curves for Ag nanotubes (*hollow symbols*) and Ag-shell silica-core (*solid line*) systems are compared. In all cases, the external radius is constant: $r_1 = 10$ nm and the internal radios r_2 is variable. *Line code* in (**a–c**) is the same as shown in (**d**)

Nanoshells and nanotubes are other example of tunable plasmonic nanostructures with important applications as nanoantennas [2, 42], light manipulators [132] and biomedical applications (http://halas.rice.edu/) [3]. Many recent studies have been focused on metallic nanoshells where the plasmon resonance can be tuned very simply by varying the shell thickness. In general, the models used to describe the response of systems with metallic shells are based on a quasi-static approximation and dipole interaction [133–137].

We focus on metallic shells with thickness from 1 to 10 nm, where the dielectric function of the metallic layer should be corrected by size [92], and the quasi-static approximation could be applicable. Results for larger systems (core radius larger than 50 nm) with thin shell layers, where the electromagnetic response is dominated by retarded effects, are also shown.

Numerical results for eigenmode excitation of metallic nanotubes corresponding to p-mode [138] are shown in Fig. 5.22 where the extinction cross section as a function of incident wavelength is depicted. For these examples and in this subsection, the external radius r_1 is constant and equal to 10 nm and the thickness ($d = r_1 - r_2$) of the nanotube is considered variable.

Figure 5.22a shows the extinction cross section for Ag nanotubes considering the dielectric function with (solid line) and without (hollow symbols) size correction.

Figure 5.22b shows the extinction cross section Au nanotubes with dielectric function thickness correction, (c) the extinction cross section for Cu nanotubes with corrected dielectric function, and (d) the extinction cross section for Ag nanotubes (hollow symbols) versus Ag/silica system (solid line) with dielectric function corrected. The inset in Fig. 5.22d shows the shell thickness code, valid also for panels (c) and (d). Hollow and solid symbols with the same color correspond to the same shell.

For these particle sizes, in general, $Q_{ext} \approx Q_{abs}$ and the extinction peaks observed in Fig. 5.7 are related with the excitation of eigenmodes. It is interesting to note that for the Ag shell, our model gives as a main result a significant widening of the resonance peak (due to the strong increase in the imaginary part of the dielectric function). The complex propagation constant solution to the homogeneous problem – eigenmode – moves away from the real axis into the complex plane as the thickness of the shell decreases. However, if the bulk dielectric function is used for all thicknesses, an opposite effect is observed: As the thickness of the shell decreases, the amplitude of the peaks increases and a more complicated evolution is observed for some cases (Au and Cu, for example). This behavior in the extinction cross-section spectra has been observed for all the examples shown in this section.

Extinction curves for Au nanotubes show a more complicated behavior. This effect can be associated to the multipole terms that play an important role for Au in the short wavelength range [137]. It can be observed in Fig. 5.22b that extinction curves for Au nanotubes present large and broad peaks for thin shells. The maximum of the extinction curves occurs for $d = 2$ nm in this configuration (see captions), while for $d = 1$ nm, the extinction peak is attenuated and strongly shifted to the IR zone. In all cases, the dipolar term dominates the extinction spectrum and the higher multipole orders have a perturbative character overlapped with the dipolar term. We can observe a similar behavior for Cu nanotubes (Fig. 5.22c) but with a more complex optical response in the short wavelength range.

In Fig. 5.22d, we compare electromagnetic response of Ag nanotubes with respect to a silica-core one ($\varepsilon_{core} = 2.25$), both with the same shell thickness. When a silica core is considered, all the spectra are shifted to the IR region, and the peaks are attenuated with respect to the same condition in the Ag nanotubes. The main cause of this shift is the relative value that the metal dielectric function takes with respect to the core dielectric constant. Therefore, the resonant coupling between surface plasmons (in both faces of the metallic shell), mainly dipolar, experiences a strong shifting to the IR zone and an intensity attenuation. This mechanism is consistent with that described by the method of hybridization [2].

Due to the size of this system (few nanometers), it is possible to compare our results with a non-retarded model. Moradi [133] proposes a non-retarded hybridization model to find the optical response of a core-shell 2D. Based on this model, it is possible to find an analytical expression to predict evolution of the peaks as a function of r_2/r_1 ratio.

In Fig. 5.23, we show the evolution of the isolated peaks of Fig. 5.22a ($\lambda_{peak} = \lambda^*$) is a function of the r_2/r_1 ratio, for both dielectric function, bulk and corrected,

Fig. 5.23 Behavior of the extinction peaks λ^* versus r_2/r_1. *Dashed lines* represent the curves computed from [133]. The numbers labeled with m correspond to the angular momentum. *Black squares* for bulk dielectric function, *red triangles* for corrected dielectric function, and *green circles* for Ag-shell silica-core 2D nanoparticles
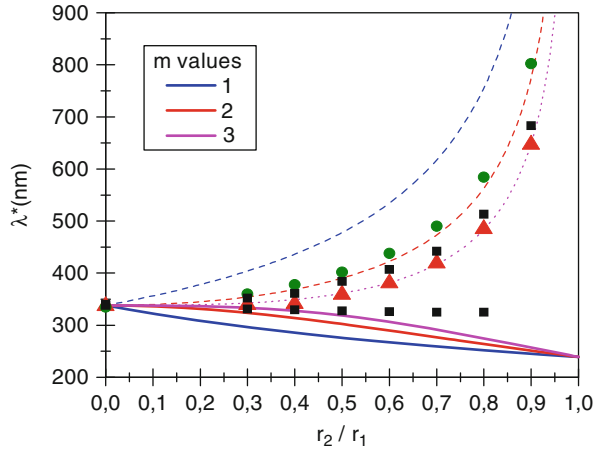

together with the silica-core metallic-shell systems (corresponding to Fig. 5.22d). In dashed lines, we show the dispersion relationship of plasmons from hybridization model corresponding to Ag nanotubes for three angular momenta m [133]. Squares and circles represent bulk dielectric function and triangles correspond to corrected dielectric function. Using the bulk dielectric function, it is possible to observe two branches, while only one branch can be detected when corrected dielectric function is used. Our calculations show that the fundamental excitation for an Ag nanotube (associated to the dipole order) dominates the extinction coefficient. In general, the principal extinction peaks follow a functional form like the predicted one by the plasmon hybridization model. The main discrepancy between the curves obtained by the non-retarded approximation and the maxima of extinction calculated by the integral method is due to the different dielectric functions used to model the systems. We observe that in the limit when $r_2 \rightarrow 0$ (solid wire), both the analytic curves and singles points (plasmonic excitations) converge to the same point.

In the quasi-static approach limit, it is possible to carry out an analysis of the interaction between eigenmodes: Eq. 6 in [133] can be rewritten in the incremental ratio form [92]:

$$\frac{\lambda_{res} - \lambda_{sp}}{\lambda_{sp}} = \frac{1}{\sqrt{1 - \left(1 - \frac{d}{r_1}\right)^m}} - 1, \tag{5.42}$$

where λ_{sp} corresponds to the wavelength for which the plasmon is excited in a solid wire with radius r_1. In this way, we can obtain a scaling law for the peaks shift that depends only on relative geometrical parameters. With this in mind, Fig. 5.24 plots $(\lambda_{peak} - \lambda_{sp})/\lambda_{sp}$ for the peak of low energy as a function of d/r_1 for different materials: Ag (circles), Au (squares), and Cu (triangles) nanotubes. Hollow symbols correspond to data extracted from Figs. 5.22a–c. In particular, for Ag nanotubes, we show in red solid circles results for a nanotube with $r_1 = 50$ nm

Fig. 5.24 Dependence of the relative shift $(\lambda_{\text{peak}} - \lambda_{\text{sp}})/\lambda_{\text{sp}}$ versus d/r_1 for the last peak eigenmode resonances for Ag (*circles*), Au (*squares*), and Cu (*triangles*) nanotubes. *Solid* and *dashed lines* correspond to the fitting curves: exponential and Eq. 5.43, for Ag nanotubes (*blue*) and Au, Cu nanotubes (*red*), respectively
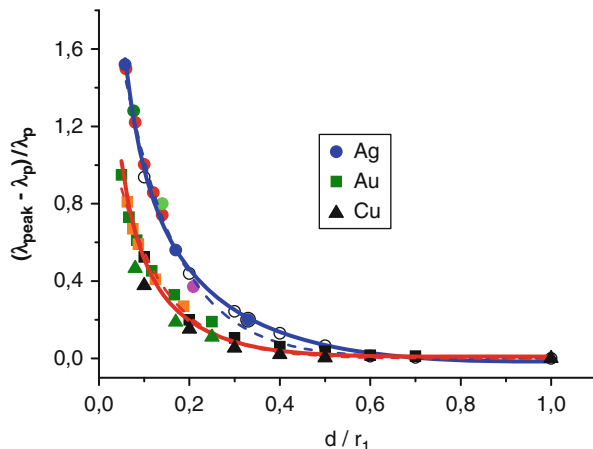
and in green circles for $r_1 = 120$ nm. The rest of the circles shown were obtained for $r_1 = 60$ nm. For Au and Cu nanotubes, we can see that the curves are very close and differ slightly from that corresponding to Ag nanotubes. In these curves, solid black symbols (squares and triangles) correspond to $r_1 = 10$ nm, the green symbols to $r_1 = 60$ nm, and orange square symbols to $r_1 = 80$ nm.

It is remarkable to note that all the points, regardless of the size of the nanotubes, can be arranged on a single curve which can be adjusted by a single-exponential decay function. A similar law was found by Jain and El-Sayed for coated spheres and dimers [134].

As a first approximation, this extinction peak is due to a dipolar interaction between plasmons. We propose a functional form for the fitting equation like Eq. 5.42 with two degrees of freedom:

$$\frac{\lambda_{res} - \lambda_{sp}}{\lambda_{sp}} = \frac{a}{\sqrt{1 - \left(1 - \frac{d}{r_1}\right)^c}} - 1 \tag{5.43}$$

The best adjustment to the black hollow circles occurs for $a = 0.988 \pm 0.005$ and $c = 2.87 \pm 0.05$ (for the complete data $a = 0.98 \pm 0.02$ and $c = 2.7 \pm 0.1$). Due to the universality of the curve, therefore, all the points can be fitted by Eq. 5.43. In Fig. 5.23, we show the two fittings: in dashed line (blue and red), the exponential law, and in solid line, the fit corresponding to Eq. 5.43.

The black square and triangle data points (corresponding to the Au and Cu $r_1 = 10$ nm) can be adjusted by the same equation (the curves of Au and Cu show little difference between them). We found that the best adjustment for the Au nanotubes occurs for $a = 1.01 \pm 0.01$ and $c = 5.6 \pm 0.2$ (solid line in Fig. 5.23). This numerical exploration in order to fit the data with the hybridization model gives as a result high values for the parameter c (equivalent to the angular momentum for the Moradi's model). This high values found for c may indicate that the

non-retarded dipole approximation is not able to describe accurately the plasmon interaction through the nanotubes walls, at least for thin shells. Recently, Encina and Coronado [139] reached a similar conclusion for dimers with Ag nanospheres, where they also observe a separation between the "universal curves" between Ag and Au dimers.

We found that the shift of the excitation peaks toward the IR is directly associated with changes in the thickness of the wall of the nanotube. In addition, the thickness of the walls modifies the constitutive parameters and, as a consequence, the plasmon–plasmon interactions. This effect is clearly seen in the Ag nanotubes. It can be observed, in particular for these structures, that the effects of retardation should be included to describe correctly the interaction between plasmons when the thickness of the layer decreases, as occurs in Ag dimers. As a result, the fractional relative plasmon curve for Ag nanotubes is separated slightly from that corresponding to Au and Cu as the shell thickness decreases and the interband transitions start to be significant. For relationships $d/r_1 > 0.6$, these effects are attenuated and the "universal curve" appears to be recovered (at least for nanotubes). The presence of a dielectric core produces perturbations in the plasmon–plasmon interaction, and the extinction peaks are shifted toward the IR zone with respect to nanotubes in the same condition. Then, the fractional plasmon shift versus d/r_1 shows a difference when nanotubes and core-shell 2D nanoparticles – for the same external radii – are compared.

In Fig. 5.25, we compare the near-field intensities, for the three structures shown in this section in the resonance condition. Figure 5.25a corresponds to the near field at $\lambda = 338$ nm for Ag circular solid nanowire with 10 nm of radius (red line extinction curve with solid circles in Fig. 5.16a). Figure 5.25b shows an intensity map for a nanotube with 10 nm of external radius and Ag wall thickness of 3 nm at $\lambda = 448$ nm (solid green curve in Fig. 5.17a). Figure 5.25c, d show the near field for the same Ag ellipsoidal nanowire (a = 10 nm, b = 60 nm), for two fundamental electric field orientations: panel (c) electric field parallel to the minor axis, resonant wavelength 329 nm; panel (d) electric field parallel to the major axis at $\lambda = 500$ nm (see red curves in Fig. 5.20a). The arrows, in all cases, indicate the direction of the incidence.

The intensity maps shown in Fig. 5.25 for the eigenmode resonances are consistent with a dipolar response (the single peak shown in the spectra of extinction curve). Due to the size of the particles considered, the scattering cross section is negligible and the entire spectrum of extinction is due to absorption. Intensifications of fields due to local resonances are very short range and can reach up to two orders of magnitude of the incident field. The resonance occupies a small volume around the nanoparticle interface, similar to a point source. This high density of field is the tool for the thermal treatment of cancer cells. In the intensity maps, we can see the field penetration inside the metal structure. Almost, the entire volume (surface) of the nanoparticle is involved in the resonant phenomenon. Thus, part of the resonant energy of free electrons can be transmitted to the structure of the metal, causing an increase in kinetic energy resulting in an increase in metal temperature [93].
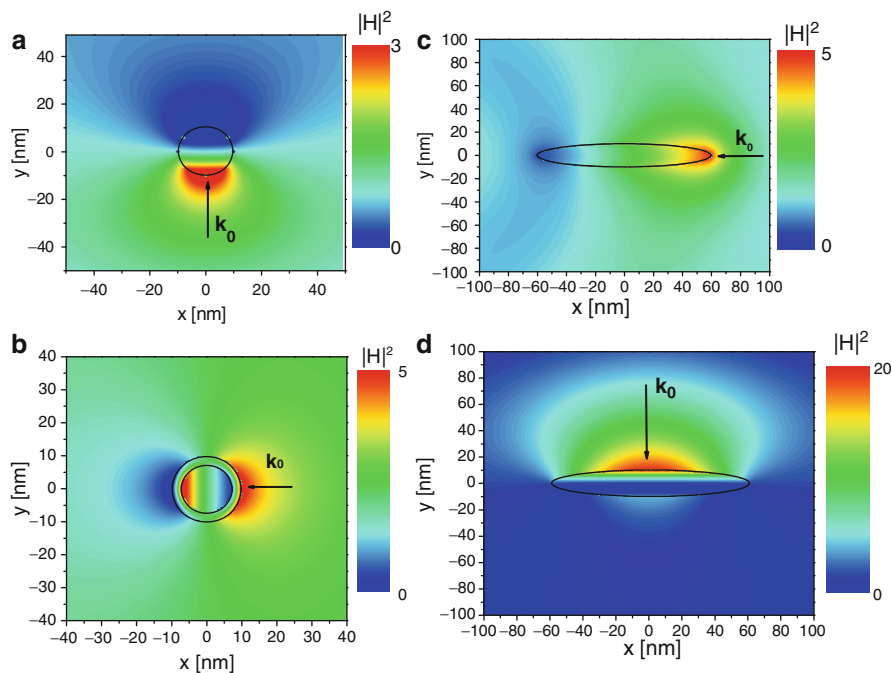
Fig. 5.25 Total near-field intensity maps $|H|^2$ (normalized to the incident intensity) for different Ag nanostructures in resonance. (**a**) *Solid circular* nanowire, $\lambda = 338$ nm, 10 nm of radius; (**b**) nanotube with 10 nm of external radius and 7 nm of the internal radius, $\lambda = 448$ nm. (**c, d**) Elliptical cross-section nanowire (aspect ratio $\mathcal{R} = 6$) for the two fundamental electric field orientations: parallel to the minor axis, $\lambda = 329$ nm and parallel to the major axis, $\lambda = 500$ nm, respectively. *Arrows* indicate the incident direction and the host medium is air

5.3.4 Experimental Results

The relation between the plasmon resonance maximum and the diameter of the spherical particle has been used by some authors as a tool to establish a range of sizes of studied metal Nps, TEM being the central technique for accurately measuring certain particles. Link et al. [140] studied laser-induced shape changes of colloidal gold nanorods after irradiating the sample with femtosecond and nanosecond laser pulses. The gold nanorods were prepared using an electrochemical method. The shape transformations of the gold nanorods are followed by two techniques: visible absorption spectroscopy by monitoring the changes in the plasmon absorption bands characteristic for gold nanoparticles and transmission electron microscopy (TEM) in order to analyze the final shape and size distribution. The extinction spectra are used to monitor the evolution of the plasmon resonances as the samples are irradiated with different pulselength lasers.

Mafuné et al. [141–147] studied the formation of noble metal (Au, Ag, and Pt) Nps under ns-regime laser ablation of solid targets in water and its relation with surfactant concentration. In all the series of papers, the authors use TEM to both

show the sphericity of the ablated Nps as well as determine their average diameter from sampling about 1,000 Nps. The extinction spectra are used to show the existence of the plasmon resonance and its dependence on different experimental parameters such as number of laser pulses, surface modifier concentration, etc.

Chen et.al [148] studied the induced alloying of Au–Pd and Ag–Pd colloidal mixtures by ns pulse laser irradiation. UV–vis absorption spectra of 1:1 and 2:1 molar ratios of Au/Pd colloidal suspensions are used to show the development of the mixture composition as a function of the laser exposure time, while the approximate sizing is performed by TEM analysis.

In a very interesting paper by Besner et al. [149], fragmentation of colloidal gold Nps by fs laser radiation is demonstrated by showing the expected blueshift of the plasmon resonance as the particle radius decreases.

In a similar way, Barcikowski and collaborators [150] study the influence of several parameters (such as pulse energy, dodecanthiol added to *n*-hexane) on gold Nps production using ultrashort pulse lasers. They show these influences by comparing extinction spectra from several treated samples, indicating the plasmon peak shift for different dodecanthiol concentrations in the liquid prior to fs laser ablation at two different laser fluences.

As a final example, Pyatenko et al. [151] produced silver nanoparticles by irradiating an Ag target with a 532 nm ns-regime laser in pure water. By working with high laser power and small spot sizes, the authors claimed to have synthesized very small spherical particles with a typical size of 2–5 nm. UV–vis extinction spectra for different beam spot sizes are used for estimating the amount of ablated Ag per pulse, according to a suggestion made by Mafuné et al. [141].

Our group has studied the relations between the different features of the extinction spectra and the size (or structure) of the Nps to use them for sizing purposes.

Scaffardi and Tocho [30] have explored the simultaneous modification of the free electron contribution to the dielectric function as well as the bound electron contribution, on the basis of Eqs. 5.11, 5.12, 5.13, 5.20, 5.38, and 5.40 to fit extinction spectra of very small nanoparticles (less than 2 nm radius). The contribution of electron transitions from the *d*-band to the conduction band was modeled using an integral expression for adding all the interband transitions across the bandgap. The dependence of the electronic density of states with size (the states begin to separate as the radius decreases) modulates the above integral expression and enables a much better fitting of the extinction spectra of very small gold nanoparticles, obtained by the inverse-micelle method. The fitting also permits the determination of microscopic parameters like the bound electron damping constant, the energy gap, and the Fermi energy of the particle.

Another application of extinction spectroscopy was developed by Roldán et al. [34], who described a method for preparation of Ag nanoparticles from chemical reduction of $AgNO_3$ in ethanol with ATS [*N*-[3-(trimethoxysilyl)propyl] diethylenetriamine] as surface modifier. While morphologic and structural characterizations of samples are conducted by Atomic Force Microscopy (AFM) and X-ray diffraction (XRD), UV–vis extinction spectroscopy interpreted through Mie theory is used to analyze the size evolution in the fabrication process of spherical silver
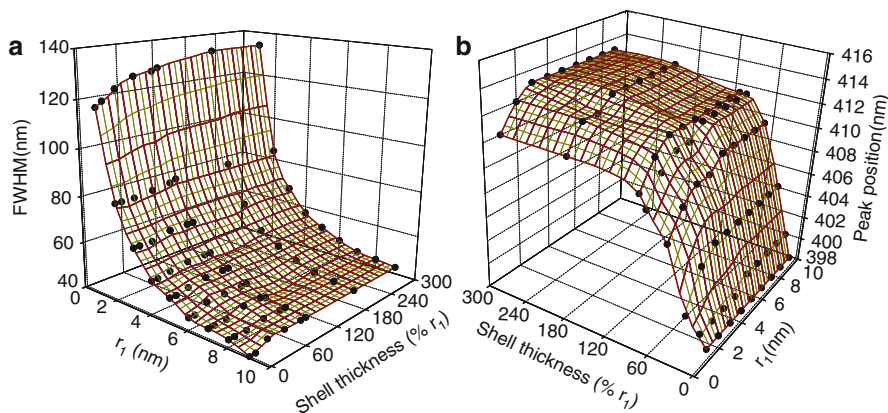
Fig. 5.26 (**a**) FWHM and (**b**) peak position of ATS-coated silver Nps immersed in ethanol as a function of core radius (r_1) and shell thickness

nanoparticles. This evolution is studied as a function of the time elapsed between the beginning of the reaction and the extraction of the sample and as a function of the temperature during the chemical reaction. The study was based on the inverse relation between the plasmon width (FWHM) and the mean radius, specially for values below 6 nm.

The optical extinction spectroscopy approach was also shown to be useful in sizing core-shell type Nps by Schinca and Scaffardi [35]. In Fig. 5.26, the authors made a detailed analysis of the dependence of plasmon resonance wavelength and FWHM with core radius and shell thickness of ATS-coated Ag Nps and were able to establish that, for sizes less than 10 nm, the plasmon peak wavelength depends almost exclusively on the shell thickness while the FWHM depends mainly on core radius. Based on these regularities, a simultaneous experimental measurement of plasmon width and plasmon peak position in extinction spectroscopy is proposed as a simple protocol for determining the mean size of noble metal core-shell nanospheres (in the size range smaller than 10 nm radius). The protocol was successfully applied to chemically and laser-ablation fabricated Ag Nps, the results of which agree with established TEM analysis.

A similar method was applied by Schinca et al. [36] to size small core-shell silver–silver oxide generated by ultrashort pulse laser ablation of solid target in water. Figure 5.27a, b show a TEM picture of the sample suspension and the corresponding size distribution histogram, respectively. In this case, the Ag Nps are capped with its own oxide during the ablation process, with a variety of thicknessess. A fit of the full experimental spectrum using Mie theory allows the determination of core size and shell thickness distributions as a function of fluence. The redshift of the plasmon peak wavelength with respect to the bare-core peak wavelength at 400 nm, produced by the oxide shell, may be easily measured even for very small thicknesses. It was found that the dominant silver oxide effective thickness is inversely proportional to the fluence, reaching a maximum of 0.2 nm
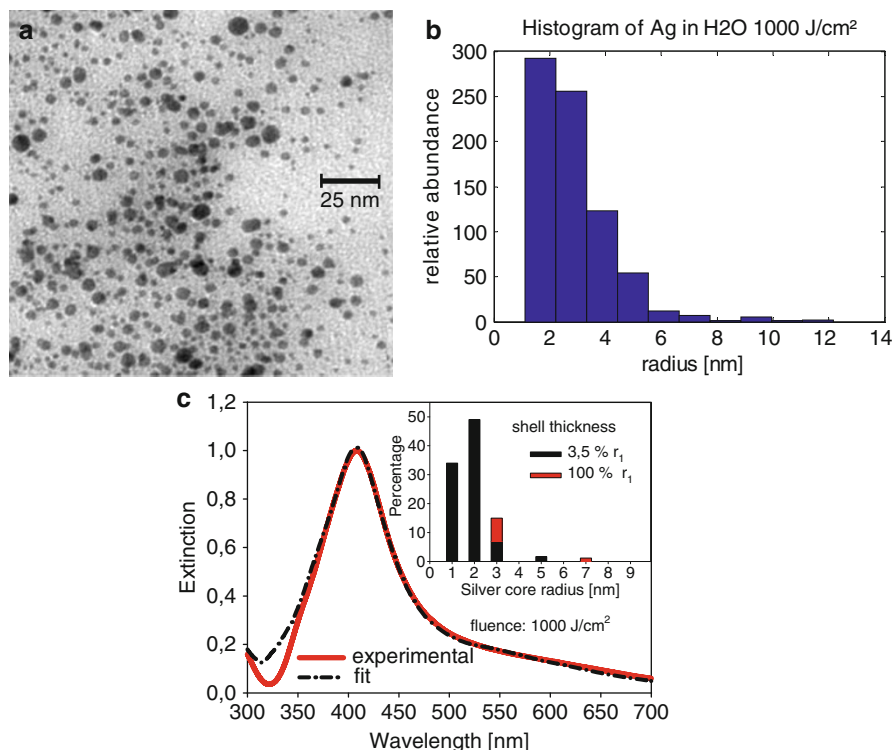
Fig. 5.27 (**a**) TEM image and (**b**) corresponding histogram of the sample of silver Nps immersed in water, fabricated at high fluence (1,000 J/cm^2); (**c**) Experimental extinction spectrum (*solid line*) and theoretical fit (*dot-dashed line*) for silver Nps in water at 1,000 J/cm^2 fluence. *Inset* shows size relative abundance distribution used for the fit

for a fluence of 60 J cm^{-2} and a minimum of 0.04 nm for a fluence of 1,000 J cm^{-2}, as it is shown in Fig. 5.27c.

For the case of Ag core-Ag$_2$O shell Nps, the relations depicted in Fig. 5.26 are a bit more complex than in the metal core dielectric shell case. Figure 5.28 shows the results of calculations of peak position (panel a), contrast (panel b) and FWHM (panel c) as a function of core radius and shell thickness. These 3D plots picture the interrelation between these three parameters. Although peak position is strongly dependent on shell thickness and almost independent of core radius, FWHM and contrast depend on both variables with similar strength. In spite of this complexity, Santillán et al. [41] have shown that a simple stepwise protocol to size oxide thickness growth over bare-core silver Np only from spectroscopic data could be devised and successfully applied to experimentally obtained single-particle extinction spectra.

Finally, the possibility of using optical extinction spectroscopy for the case of metal coated dielectric core Nps is also evident when the relation between the FWHM and peak resonance position as a function of core radius and shell thickness is analyzed. Figure 5.29 plots these relations for the case of a silica core and Ag shell.
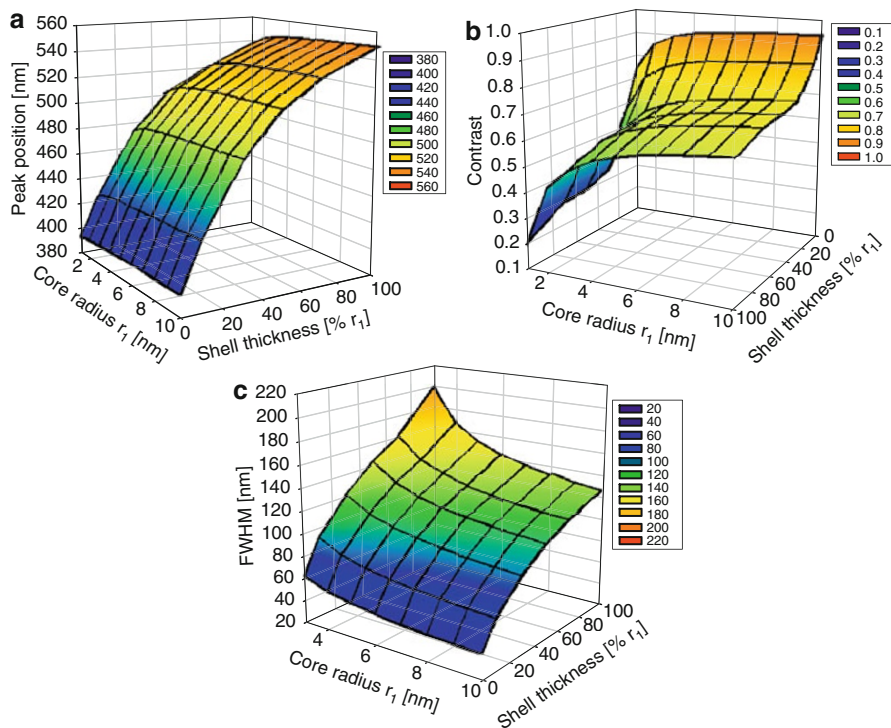
Fig. 5.28 (**a**) Plasmon peak wavelength, (**b**) Contrast and (**c**) FWHM as a function of core radius and shell thickness for Ag–Ag$_2$O core-shell Nps in water
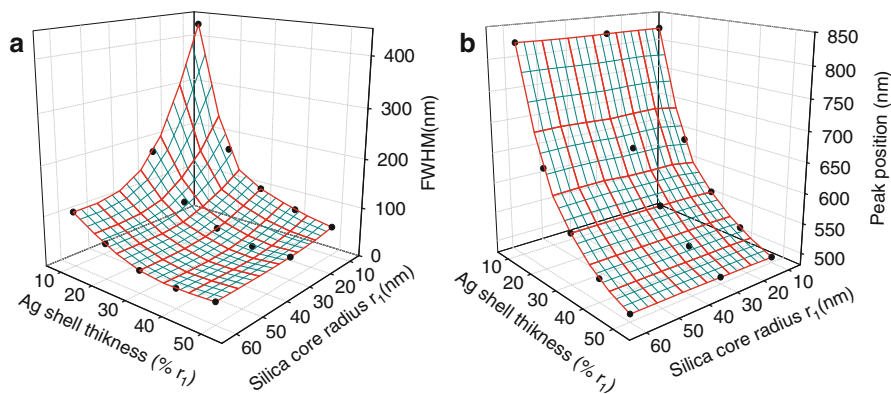

Fig. 5.29 (**a**) FWHM and (**b**) peak position of Ag-coated silica-core Nps immersed in ethanol as a function of core radius (r_1) and shell thickness

It can be seen that the peak position (panel b) is still strongly dependent on metal shell thickness and almost independent of silica-core radius, but FWHM depends on both Ag-shell thickness and silica-core radius. In this case, a measurement protocol may also be devised to size separately the core radius and metal shell thickness of single core-shell nanoparticles. These two last cases are important since researchers in the biological area are directing their interest in developing single-particle nanosensors for intracellular measurement of oxidative processes [152, 153].

6   Conclusions and Future Perspective

Throughout this chapter, we have shown results referring to the optical response of infinitely long metallic wires with cross section of the order of a few nanometers. The theoretical and numerical results suggest the concrete possibility of controlling this optical response with an appropriate engineering of nanoparticles. The relation of the constitutive parameters with particle size, coupled with interband transitions in the metal, gives a correct description of the experimentally measured optical observables. Our theoretical results show a slight blueshift of the resonance peak (for p-polarization) as the particle size decreases (most notorious for Ag nanowires).

The dependence of dielectric function on the particle size generates an anisotropy with the polarization of the incident wave: The size correction begins to be necessary for radii of the order of 7 nm and when the electric field vector is parallel to the cross section. This sensitivity of the eigenmodes with the orientation of the electric field can also be observed when the cross-sectional geometry deviates from the perfect circular symmetry. For the example studied in this work, oblong particles (two main axes), the orientation of the electric field determines two plasmonic resonances. The design of the geometry of the particle can "tune in" two-channel resonance. One channel is shifted to the blue and the other with a greater range of variability to the red (compared to the position of the plasmon for circular particle). Responsible for such behavior is an anisotropic tensor polarization induced by external fields.

The geometry of the nanoparticle and the surrounding medium significantly influence the optical response. A mixture of both conditions, along with size corrected dielectric function, can yield systems with multiple plasmonic excitations with redshifts of the resonant peak. While the physical principles involved in the electromagnetic interaction with the metal layer are the same (the excitation of free electrons), now couplings between resonant eigenmodes generated on both sides of the shell exist. This plasmon coupling reminds the orbital electronic coupling in diatomic molecules. The resonant couplings of the eigenmodes can be estimated in the small-particle limit, using a hybrid mix of "wave functions": eigenmodes corresponding to a solid particle with corresponding eigenmodes in a cavity. The interactions between surface plasmons generated on both sides of the metal shell determine the resonant channel, with possible shifts of the resonance peak toward blue or red.

The understanding of the physical mechanisms involved in the optical response of nanoscale systems (which results in the ability to "tune" these eigenmodes through the design of structures) opens a large number of practical applications. Today, these applications seem to be focusing strongly on biomedicine (optical tracers, heat treatment of tumors [93]), optical communications (plasmon waveguide-based nanocircuitry, optical antennas [4, 154]), and engineering of solar cells [155].

References

1. Yogeswaran U, Chen S-M (2008) A review on the electrochemical sensors and biosensors composed of nanowires as sensing material. Sensors 8:290–313
2. Halas NJ, Lal S, Chang W-S, Link S, Nordlander P (2011) Plasmons in strongly coupled metallic nanostructure. Chem Rev 111:3913–3961
3. Hirsch L et al (2006) Metal nanoshells. Ann Biomed Eng 34:15–22
4. Giannini V, Fernández-Domínguez AI, Heck SC, Maier SA (2011) Plasmonic nanoantennas: fundamentals and their Use in controllingthe radiative properties of nanoemitters. Chem Rev 111:3888–3912
5. Brambilla G (2010) Optical fibre nanowires and microwires: a review. J Opt 12:043001, 1–19
6. Macwan DP, Dave PN, Chaturvedi S (2011) A review on nano-TiO$_2$ sol–gel type syntheses and its applications. J Mater Sci 46:3669–3686
7. Huang X, El-Sayed MA (2010) Gold nanoparticles: optical properties and implementations in cancer diagnosis and photothermal therapy. J Adv Res 1:13–28
8. Wang W, Yang Q, Fan F, Hongxing X, Wang ZL (2011) Light propagation in curved silver nanowire plasmonic waveguides. Nano Lett 11:1603–1608
9. Ma L-C, Zhang Y, Zhang J-M, Ke-Wei X (2011) First-principles study on structural and electronic properties of copper nanowire encapsulated into GaN nanotube. Physica B 406:3502–3507
10. Long Y-Z, Li M-M, Changzhi G, Wan M, Duvail J-L, Liu Z, Fan Z (2011) Recent advances in synthesis, physical properties and applications of conducting polymer nanotubes and nanofibers. Prog Polym Sci 36:1415–1442
11. Barnard ES, Pala RA, Brongersma ML (2011) Photocurrent mapping of near-field optical antenna resonances. Nat Nanotechnol 6:588–593
12. Makino K, Tominaga J, Hase M (2011) Ultrafast optical manipulation of atomic arrangements in chalcogenide alloy memory materials. Opt Express 19:1260–1270
13. Alekseeva AV, Bogatyrev VA, Dykman LA, Khlebtsov BN, Trachuk LA, Melnikov AG, Khlebtsov NG (2005) Preparation and optical scattering characterization of gold nanorods and their application to a dot-immunogold assay. Appl Opt 49:6285–6295
14. Encina ER, Coronado EA (2007) Resonance conditions for multipole plasmon excitations in noble metal nanorods. J Phys Chem C 111(45):16796–16801
15. Perassi EM, Hernandez-Garrido JC, Moreno MS, Encina ER, Coronado EA, Midgley PA (2010) Using highly accurate 3D nanometrology to model the optical properties of highly irregular nanoparticles: a powerful tool for rational design of plasmonic devices. Nano Lett 10:2097–2104

16. Scaffardi LB, Pellegri N, de Sanctis O, Tocho LO (2005) Sizing gold nanoparticles by optical extinction spectroscopy. Nanotechnology 16:158–163
17. Mahmoud MA, Snyder B, El-Sayed MA (2010) Surface plasmon fields and coupling in the hollow gold nanoparticles and surface-enhanced Raman spectroscopy. Theory and experiment. J Phys Chem C 114:7436–7443
18. Ferrara MA, Rendina I, Basu SN, Dal Negro L, Sirleto L (2012) Raman amplifier based on amorphous silicon nanoparticles. Int J Photoenergy 2012:254946, 1–5
19. Eustis S, El-Sayed MA (2006) Determination of the aspect ratio statistical distribution of gold nanorods in solution from a theoretical fit of the observed inhomogeneously broadened longitudinal plasmon resonance absorption spectrum. J Appl Phys 100:044324, 1–7
20. Jian Z, Junwu Z, Yongchang W (2004) Influence of surface charge density on the plasmon resonance modes in gold nanoellipsoid. Physica B 353:331–335
21. Zhu J (2005) Shape dependent full width at half maximum of the absorption band in gold nanorods. Phys Lett A 339:466–471
22. Khlebtsov B, Khanadeev V, Pylaev T, Khlebtsov NA (2011) New T-matrix solvable model for nanorods: TEM-based ensemble simulations supported by experiments. J Phys Chem C 115:6317–6323
23. Encina ER, Perassi EM, Coronado EA (2009) Near-field enhancement of multipole plasmon resonances in Ag and Au nanowires. J Phys Chem A 113:4489–4497
24. Pavlovic G, Malpuech G, Gippius NA (2010) Dispersion and polarization conversion of whispering gallery modes in nanowires. Phys RevB 82:195328, 1–8
25. Scaffardi LB, Lester M, Skigin D, Tocho JO (2007) Optical extinction spectroscopy used to characterize metallic nanowires. Nanotechnology 18:315402, 1–8
26. Brambilla G (2010) Accurate 3D nanometrology to model the optical properties of highly irregular nanoparticles: a powerful tool for rational design of plasmonic devices. Nano Lett 10:2097–2104
27. Kottmann JP, Martin OJF, Smith DR, Schultz S (2000) Field polarization and polarization charge distributions in plasmon resonant particles. New J Phys 2:271–279
28. Scaffardi L, Tocho JO, Yebrin L, Cantera C (1996) Sizing particles used in the leather industry by light scattering. Opt Eng 35(1):52–56
29. Garcés Vernier I, Sotolongo O, Hernández MP, Scaffardi L, García-Ramos JV, Rivas L (2000) Determination of particle size distribution of particles on aerosols and suspensions by ultraviolet–visible-near infrared absorbance measurements. A new procedure for absorbing particles. Phys Status Solid B 220:583–586
30. Scaffardi LB, Tocho JO (2006) Size dependence of refractive index of gold nanoparticles. Nanotechnology 17:1309–1315
31. Scaffardi LB, Lester M, Skigin D, Tocho JO (2007) Optical extinction spectroscopy used to characterize metallic nanowires. Nanotechnology 18:315402–315410
32. Scaffardi LB, Tocho JO (2008) Absorption spectra of tiny gold and silver objects. J Luminisc 128(5–6):828–830
33. Torchia GA, Scaffardi LB, Méndez C, Moreno P, Tocho JO, Roso L (2008) Optical extinction for determining size distribution of gold nanoparticles fabricated by ultrashort pulsed laser ablation. Appl Phys A Mater Sci Process 93(4):967–971
34. Roldán MV, Scaffardi LB, de Sanctis O, Pellegri N (2008) Optical properties and extinction spectroscopy to characterize the synthesis of amine capped silver nanoparticles. Mater Chem Phys 112:984–990
35. Schinca DC, Scaffardi LB (2008) Core and shell sizing of small silver coated nanospheres by optical extinction spectroscopy. Nanotechnology 19:495712–495720
36. Schinca DC, Scaffardi LB, Videla FA, Torchia GA, Moreno P, Roso L (2009) Silver-silver oxide core-shell nanoparticles by femtosecond laser ablation. Characterization by extinction spectroscopy. J Phys D: Appl Phys 42:215102–215111
37. Videla FA, Torchia GA, Schinca DC, Scaffardi LB, Moreno P, Méndez C, Roso L, Giovanetti L, Lopez JR (2009) Role of supercontinuum in the fragmentation of colloidal gold nanoparticles in solution. Proc SPIE 7405:74050U-1–74050U-12

38. Videla FA, Torchia GA, Schinca DC, Scaffardi LB, Moreno P, Mendez C, Giovanetti L, Ramallo López J, Roso L (2010) Analysis of the main optical mechanisms responsible for fragmentation of gold nanoparticles by femtosecond laser radiation. J Appl Phys 107:114308-1–114308-8

39. Santillán JMJ, Scaffardi LB, Schinca DC, Videla FA (2010) Determination of nanometric Ag_2O film thickness by surface plasmon resonance and optical waveguide mode coupling techniques. J Opt 12:045002–045010

40. Videla FA, Torchia GA, Schinca DC, Scaffardi LB, Moreno P, Méndez C, Giovanetti LJ, RamalloLopez JM, Roso L (2010) Analysis of the main optical mechanisms responsible for fragmentation of gold nanoparticles by femtosecond laser radiation. Virtual J Sci Technol Ultrafast Sci Sect Photonics 9(7)

41. Santillán JMJ, Scaffardi LB, Schinca DC (2011) Quantitative optical extinction-based parametric method for sizing a single core–shell $Ag–Ag_2O$ nanoparticle. J Phys D: Appl Phys 44:105104–105112

42. Abraham Ekeroth RM, Lester M, Scaffardi LB, Schinca DC (2011) Metallic nanotubes characterization via surface plasmon excitation. Plasmonics 6(3):435–444

43. Coronado E, Schatz G (2003) Surface plasmon broadening for arbitrary shape nanoparticles: a geometrical probability approach. J Chem Phys 7:3926–3934

44. Kottmann JP, Martin OJF (2001) Influence of the cross section and the permittivity on the plasmon-resonance spectrum of silver nanowires. Appl Phys B 73:299–304

45. Ranjan M, Oates TW, Facsko S, Mller W (2010) Optical properties of silver nanowire arrays with 35 nm periodicity. Opt Lett 35:2576–2578

46. Brack M (1993) The physics of simple metal clusters: self-consistent jellium model and semiclassical approaches. Rev Mod Phys 3:677–732

47. Bonacic-Koutecky V, Piercarlo Fantucci J, Koutecky J (1991) Quantum chemistry of small clusters of elements of groups Ia, Ib, and IIa: fundamental concepts, predictions, and interpretation of experiments. Chem Rev 91:1035–1108

48. Bohren CF, Huffman DR (1983) Absorption and scattering of light by small particles. Wiley, New York

49. Lorentz HA (1905) The motion of electrons in metallic bodies. Proc R Acad Sci Amst 7:438, 585, 684

50. (a) Drude P (1900) The theory of metals ions. Phys Zeitsch 1:161; (b) Drude P (1900) Zur elektronentheori der metalles 1 Teil. Ann Phys (Leipzig) 1:566

51. Kreibig U, Vollmer M (1995) Optical properties of metal clusters. Springer, Berlin

52. Kraus WA, Schatz GC (1983) Plasmon resonance broadening in small metal particles. J Chem Phys 79:6130–6139

53. Kraus WA, Schatz GC (1983) Plasmon resonance broadening in spheroidal metal particles. J Chem Phys 99:353–357

54. Doyle WT (1958) Absorption of light by colloids in alkali halide crystals. Phys Rev 111:1097–1077

55. (a) Genzel L, Martin TP, Kreibig U (1975) Dielectric function and plasma resonances of small metal particles, Z Physik B 21:339. http://www.springerlink.com/content/j2885x1521060275/; (b) Ruppin R, Yatom H (1976) Size and Shape Effects on the Broadening of the Plasma Resonance Absorption in Metals, Phys Status Solid B 74:647; (c) Wood DM, Ashcroft NW (1982) Quantum size effects in the optical propertiesof small metallic particles, Phys Rev B 25:6255; (d) Apell P, Penn DR (1983) Optical Properties of Small Metal Spheres:surface Effects, Phys Rev Lett 50:1316–1319

56. Granqvist CG, Hunderi O (1977) Optical properties of ultra fine gold particles. Phys Rev B 16:3513–3534

57. Palik ED (1985) Handbook of optical constants of solids. Academic, San Diego

58. Johnson PB, Christy RW (1972) Optical constants of noble metals. Phys Rev B 6:4370–4379

59. Pinchuk A, von Plessen G, Kreibig U (2004) Influence of interband electronic transitions on the optical absorption in metallic nanoparticles. J Phys D: Appl Phys 37:3133–3139

60. Rosei R, Antonangeli F, Grassano UM (1973) d bands position and width in gold from very low temperature thermomodulation measurements. Surf Sci 37:689–699
61. Novotny L, Hecht B (2006) Principles of nano-optics. Cambridge University Press, Cambridge
62. Maier S (2006) Plasmonic: metal nanoetructures for subwavelength photonic devices. IEEE J Sel Top Quantum Electron 12:1214–1220
63. Kreibig U (1970) Kramers kronig analysis of the optical properties of small silver particles. Z Phys 234:307–318
64. Kreibig U, Fragstein CV (1969) The limitation of electron mean free path in small silver particles. Z Phys 224:307–323
65. Rosei R (1974) Temperature modulation of the optical transitions involving the Fermi surface in Ag: theory. Phys Rev B 10:474–483
66. Inouye H, Tanaka K, Tanahashi I, Hirao K (1998) Ultrafast dynamics of nonequilibrium electrons in a gold nanoparticles system. Phys Rev B 57:11334–11340
67. Cain W, Shalaev V (2010) Optical metamaterials: fundamental and applications. Springer, Heidelberg
68. Santillán JMJ, Videla FA, Scaffardi LB, Schinca DC (2012) Plasmon spectroscopy for subnanometric copper particles: dielectric function and core-shell sizing. Plasmonics 1–8, doi:10.1007/s11468-012-9395-8
69. Logunov SL, Ahmadi TS, El-Sayed MA, Khoury JT, Whetten RL (1997) Electron dynamics of passivated gold nanocrystals probed by subpicosecond transient absorption spectroscopy. J Phys Chem B 101:3713–3719
70. Boyen H-G, Kästle G, Weigl F, Koslowski B et al (2002) Oxidation-resistant gold-55 clusters. Science 30:1533–1536
71. van de Hulst HC (1981) Light scattering by small particles. Dover, New York
72. Jackson JD (1999) Classical electrodynamics, 3rd edn. Wiley, New York
73. Zhao J, Pinchuk AO, McMahon JM, Li S, Ausman LK, Atkinson AL, Schatz GC (2008) Methods for describing the electromagnetic properties of silver and gold nanoparticles. Acc Chem Res 41(12):1710–1720
74. Kelly KL, Coronado E, Zhao LL, Schatz GC (2003) The optical properties of metal nanoparticles: the influence of size, shape, and dielectric environment. J Phys Chem B 107:668–677
75. Born M, Wolf E (1999) Principles of optics. Cambridge University Press, Cambridge
76. Ishimaru A (1997) Wave propagation and scattering in random media. IEEE Press/Oxford University, New York/Oxford
77. Straton JA (1941) Electromagnetic theory. Mc Graw-Hills, New York
78. Raether H (1988) Surface plasmons on smooth and rough surfaces and on grattings, vol 111, Springer tracts in modern physics. Springer, Berlin
79. Wokaun AW (1984) Surface enhanced electromagnetic processes. Solid State Phys 38:223–294
80. Pedersen TG, Jung J, Søndergaard T, Pedersen K Nanopar (2011) Nanoparticle plasmon resonances in the near-static limit. Optics Letters 36(5):713–715
81. Purcell EM, Pennypacker CR (1973) Scattering and absorption of light by non-spherical dielectric grains. Astrophys J 186:705
82. Miller EK (1994) Time domain modelling in electromagnetics. J Electromagn Waves Appl 8:1125–1172
83. Jerez S, Lara A (2011) A high resolution nonstandard FDTD method for the TM mode of Maxwell's equations. Math Comput Model 54:1852–1857
84. Hafner C, Ballist R (1983) The multiple multipole method (MMP). Int J Comput Electr Electron Eng 2:1–7
85. Pendry JB, MacKinnon A (1992) Calculation of photon dispersion relations. Phys Rev Lett 69:2772–2775
86. Khlebtsov B, Khanadeev V, Pylaev T, Khlebtsov N (2011) A new T-matrix solvable model for nanorods: TEM-based ensemble simulations supported by experiments. J Phys Chem C 115:6317–6323

87. (a) Jin J (2002) The finite element method in electromagnetics. Wiley, New York. (b) Nieto-Vesperinas M (1991) Scattering and diffraction in physical optics. Wiley, New York (Chaps 1 and 7)
88. Madrazo A, Nieto-Vesperinas M (1995) Scattering of electromagnetic waves from a cylinder in front of a conducting plane. J Opt Soc Am A 12:1298–1309
89. Lester M, Nieto-Vesperinas M (1999) Optical forces on microparticles in an evanescent laser field. Opt Lett 26:936–938
90. Lester M, Arias-González JR, Nieto-Vesperinas M (2001) Fundamentals and model of photonic-force microscopy. Opt Lett 26:707–709
91. Arias-González de la Aleja JR (2002) Electromagnetic resonances in the light scattering by objects and surfaces. Ph.D. thesis, Universidad Complutense de Madrid, Spain. ISBN: 84-669-1863-9. http://www.ucm.es/BUCM/tesis/fis/ucm-t26131.pdf
92. Abraham Ekeroth RM, Lester M, Scaffardi LB, Schinca DC (2011) Metallic nanotubes characterization via surface plasmon excitation. Plasmonics 6:435–444
93. Huang X, Jain PK, El-Sayed IH, El-Sayed MA (2008) Plasmonic photothermal therapy (PPTT) using gold nanoparticles. Lasers Med Sci 23:217–228
94. Huang X, Neretina S, El-Sayed MA, Nanorods G (2009) From synthesis and properties to biological and biomedical applications. Adv Mater 21:4880–4910
95. Pérez-Juste J, Pastoriza-Santos I, Liz-Marzán LM, Mulvaney P (2005) Gold nanorods: synthesis, characterization and applications. Coord Chem Rev 249:1870–1901
96. Moskovits M (1985) Surface-enhanced spectroscopy. Rev Mod Phys 57:783–826
97. Oates TWH, Sugime H, Noda S (2009) Combinatorial surface-enhanced Raman spectroscopy and spectroscopic ellipsometry of silver island films. J Phys Chem C 113:4820–4828
98. Aroca R (2006) Surface-enhanced vibrational spectroscopy. Wiley, Hoboken
99. Kneipp K, Wang Y, Kneipp H, Perelman LT, Itzkan I, Dasari RR, Feld MS (1997) Single molecule detection using surface-enhanced Raman scattering (SERS). Phys Rev Lett 78:1667–1670
100. Emory SR, Nie S (1997) Near-field surface-enhanced Raman spectroscopy on single silver nanoparticles. Anal Chem 69:2631–2635
101. Xu H, Bjerneld EJ, Kall M, Börjesson L (1999) Spectroscopy of single enhanced Raman scattering. Phys Rev Lett 83:4357–4360
102. Elghanian R, Storhoff JJ, Mucic RC, Letsinger RL, Mirkin CA (1997) Selective colorimetric detection of polynucleotides based on the distance-dependent optical properties of gold nanoparticles. Science 277:1078–1081
103. Lyon LA, Musick MD, Natan MJ (1998) Colloidal Au-enhanced surface plasmon resonance immunosensing. Anal Chem 70:5177–5183
104. Schultz S, Smith DR, Mock JJ, Schultz DA (2000) Single-target molecule detection with nonbleaching multicolor optical immunolabels. Proc Natl Acad Sci USA 97:996–1001
105. Sönnichsen C, Geier S, Hecker NE, von Plessen G, Feldmann J, Ditlbacher H, Lamprecht B, Krenn JR, Aussenegg FR, Chan VZ-H, Spatz JP, Möller M (2000) Spectroscopy of single metallic nanoparticles using total internal reflection microscopy. Appl Phys Lett 77:2949–2952
106. Specht M, Pedarnig JD, Heckl WM, Hänsch TW (1992) Scanning plasmon near-field microscope. Phys Rev Lett 68:476–479
107. Inouye Y, Kawata S (1994) Near-field scanning optical microscope with a metallic probe tip. Opt Lett 19:159–161
108. Hecht B, Sick B, Wild UP, Deckert V, Zenobi R, Martin OJF, Pohl DW (2000) Scanning near-field optical microscopy with aperture probes: fundamentals and applications. J Chem Phys 112:7761–7775
109. Stöckle RM, Suh YD, Deckert V, Zenobi R (2000) Nanoscale chemical analysis by tip-enhanced Raman spectroscopy. Chem Phys Lett 318:131–136
110. Sqalli O, Bernai MP, Hoffmann P, Marquis-Weible F (2000) Improved tip performance for scanning near-field optical microscopy by the attachment of a single gold nanoparticle. Appl Phys Lett 76:2134–2137

111. Milner RG, Richards D (2001) The role of tip plasmons in near-field Raman microscopy. J Microsc 202:66–71

112. Manjavacas A, García de Abajo FJ (2009) Robust plasmon waveguides in strongly interacting nanowire arrays. Nano Lett 9:1285–1289

113. Vogelgesang R, Dorfmüller J, Esteban R, Weitz RT, Dmitriev A, Kern K (2008) Plasmonic nanostructures in apertureless scanning near-field optical microscopy (aSNOM). Phys Status Solid B 245:2255–2260

114. Dickson RM, Lyon LA (2000) Unidirectional plasmon propagation in metallic nanowires. J Phys Chem B 104:6095–6098

115. Fang Z, Fan L, Lin C, Zhang D, Meixner AJ, Zhu X (2011) Plasmonic coupling of bow tie antennas with Ag nanowire. Nano Lett 11:1676–1680

116. Quinten M, Leitner A, Krenn JR, Aussenegg FR (1998) Electromagnetic energy transport via linear chains of silver nanoparticles. Opt Lett 23:1331–1333

117. Krenn JR, Dereux A, Weeber JC, Bourillot E, Lacroute Y, Goudonnet JP (1999) Squeezing the optical near-field zone by plasmon coupling of metallic nanoparticles. Phys Rev Lett 82:2590–2593

118. Bozhevolnyi SI, Erland J, Leosson K, Skovgaard PMW, Hvam JM (2001) Waveguiding in surface plasmon polariton band gap structures. Phys Rev Lett 86:3008–3011

119. Weeber J-C, Dereux A, Girard C, Krenn JR, Goudonnet J-P (1999) Plasmon polaritons of metallic nanowires for controlling submicron propagation of light. Phys Rev B 60:9061–9068

120. Lamprecht B, Schider G, Lechner RT, Ditlbacher H, Krenn JR, Leitner A, Aussenegg FR (2000) Metal nanoparticle gratings: influence of dipolar particle interaction on the plasmon resonance. Phys Rev Lett 84:4721–4724

121. Brongersma ML, Hartman JW, Atwater HA (2000) Electromagnetic energy transfer and switching in nanoparticle chain arrays below the diffraction limit. Phys Rev B 62:R16356–R16359

122. Krenn JR, Salerno M, Felidj N, Lamprecht B, Schider G, Leitner A, Aussenegg FR, Weeber JC, Dereux A, Goudonnet JP (2001) Light field propagation by metal micro- and nanostructures. J Microscopy 202:122–128

123. Lester M, Skigin D (2007) Coupling of evanescent s-polarized waves to the far field by waveguide modes in metallic arrays. J Opt A Pure Appl Opt 9:81–87

124. Skigin D, Letser M (2011) Optical nanoantennas: from comminications to super-resolution. J Nanophotonics 5:050303, 1–3

125. Martin-Moreno L, García-Vidal FJ, Lezec HJ, Pellerin KM, Thio T, Pendry JB, Ebbesen TW (2001) Theory of extraordinary optical transmission through subwavelength hole arrays. Phys Rev Lett 86:1114–1117

126. Lester M, Skigin D (2011) An optical nanoantenna made of plasmonic chain resonators. J Opt 13:035105–0345113

127. Barnard ES, Pala RA, Brongersma ML (2011) Photocurrent mapping of near-field optical antenna resonances. Nat Nanotechnol 6:588–593

128. Tominaga J, Mihalcea C, Büchel D, Fukuda H, Nakano T, Atoda N, Fuji H, Kikukawa T (2001) Local plasmon photonic transistor. Appl Phys Lett 78:2417–2420

129. Link S, El-Sayed MA (2000) Shape and size dependence of radiative, non-radiative and photothermal properties of gold nanocrystals. Int Rev Phys Chem 19:409–453

130. Santillán JMJ, Scaffardi LB, Schinca DC (2011) Quantitative optical extinction based parametric method for sizing a single core-shell Ag–Ag_2O nanoparticle. J Phys D: Appl Phys 44:105104, 1–8

131. Novotny L, van Hulst N (2011) Antennas for light. Nat Photonics 5:83–90

132. Silveirinha MG, Alu A, Engheta N (2008) Cloaking mechanism with antiphase plasmonic satellites. Phys Rev B 78:205109–205118

133. Moradi A (2008) Plasmon hybridization in metallic nanotubes. J Phys Chem Solid 69:2936–2838

134. Jain PK, El-Sayed MA (2007) Universal scaling of plasmon coupling in metal nanoestructures: extension from particles pair to nanoshells. Nano Lett 9:2854–2858

135. Park T, Nordlander P (2009) On the nature of the bonding and antibonding metallic film and nanoshell plasmons. Chem Phys Lett 472:228–231

136. Zhu J (2007) Theoretical study of the tunable second-harmonic generation (SHG) enhancement factor of gold nanotubes. Nanotechnology 18:225702

137. Wu D, Xu X, Liu X (2008) Influence of dielectric core, embedding medium and size on the optical properties of gold nanoshells. Solid State Commun 146:7–11

138. Calculations of cross sections in this section were performed with the integrated method outlined in Section 2, extended to cover the case of cylinders coated. For details of the method see [92]

139. Encina E, Coronado E (2010) Plasmon coupling in silver nanosphere pairs. J Phys Chem C 114:3918–3923

140. Link S, Burda C, Nikoobakht B, El-Sayed MA (2000) Laser-induced shape changes of colloidal gold nanorods using femtosecond and nanosecond laser pulses. J Phys Chem B 104(26):6152–6163

141. Mafuné F, Kohno J-y, Takeda Y, Kondow T, Sawabe H (2000) Structure and stability of silver nanoparticles in aqueous solution produced by laser ablation. J Phys Chem B 104(35):8333–8337

142. Mafuné F, Kohno J-y, Takeda Y, Kondow T (2002) Full physical preparation of size-selected gold nanoparticles in solution: laser ablation and laser-induced size control. J Phys Chem B 106(31):7575–7577

143. Mafuné F, Kohno J-y, Takeda Y, Kondow T, Sawabe H (2001) Formation of gold nanoparticles by laser ablation in aqueous solution of surfactant. J Phys Chem B 105:5114–5120

144. Mafuné F, Kohno J-y, Takeda Y, Kondow T, Sawabe H (2000) Formation and size control of silver nanoparticles by laser ablation in aqueous solution. J Phys Chem B 104:9111–9117

145. Mafuné F, Kohno J-y, Takeda Y, Kondow T (2002) Growth of gold clusters into nanoparticles in a solution following laser-induced fragmentation. J Phys Chem B 106:8555–8561

146. Mafuné F, Kohno J-y, Takeda Y, Kondow T (2001) Dissociation and aggregation of gold nanoparticles under laser irradiation. J Phys Chem B 105:9050–9056

147. Mafuné F, Kohno J-y, Takeda Y, Kondow T (2003) Formation of stable platinum nanoparticles by laser ablation in water. J Phys Chem B 107:4218–4223

148. Chen Y-H, Tseng Y-H, Yeh C-S (2002) Laser-induced alloying Au–Pd and Ag–Pd colloidal mixtures: the formation of dispersed Au/Pd and Ag/Pd nanoparticle. J Mater Chem 12:1419–1422

149. Besner S, Kabashin AV, Meunier M (2006) Fragmentation of colloidal nanoparticles by femtosecond laser-induced supercontinuum generation. Appl Phys Lett 89:233122–233125

150. Hahn A, Barcikowski S, Chichkov BN (2008) Influences on nanoparticle. Production during pulsed laser ablation. J Laser Micro/Nanoeng 3(2):73–77

151. Pyatenko A, Shimokawa K, Yamaguchi M, Nishimura O, Suzuki M (2004) Synthesis of silver nanoparticles by laser ablation in pure water. Appl Phys A 79:803–806

152. Novo C, Funston AM, Mulvaney P (2008) Direct observation of chemical reactions on single gold nanocrystals using surface plasmon spectroscopy. Nat Nanotechnol 3:598–602

153. Anker JN, Paige Hall W, Lyandres O, Shah N, Zhao J, Van Duyne R (2008) Biosensing with plasmonic nanosensors. Nat Mater 7:442–453

154. Alù A, Young M, Engheta N (2008) Design of nanofilter for optical nanocircuits. Phys Rev B 77:144107–144119

155. Cao L, Fan P, Vasudev AP, White JS, Yu Z, Cai W, Schuller JA, Fan S, Brongersma ML (2010) Semiconductor nanowire optical antenna solar absorbers. Nano Lett 10:439–445